Chemical Engineering Journal 487 (2024) 150461

Contents lists available at ScienceDirect

Chemical Engineering Journal

journal homepage: www.elsevier.com/locate/cej

Dynamic bubble tracking in fluidized beds via electrical capacitance volume tomography

Brigham Watson [a], Lennard Lindmüller [a,*], Stefan Heinrich [a], Jörg Theuerkauf [b], Yuan Yao [c], Yi Fan [c]

[a] Hamburg University of Technology, Institute of Solids Process Engineering and Particle Technology, Denickestraße 15, 21073 Hamburg, Germany
[b] Engineering and Process Science, Core R&D, The Dow Chemical Company, Midland, MI, USA
[c] Engineering and Process Science, Core R&D, The Dow Chemical Company, Lake Jackson, TX, USA

ARTICLE INFO

Keywords:
Fluidization
Fluidized bed
Electrical capacitance volume tomography
Bubble detection
Bubble properties
Multiphase systems

ABSTRACT

This work sets forth the development of a novel, dynamic bubble detection algorithm for use with electrical capacitance volume tomography (ECVT) sensors for bubbling fluidized beds. Starting with an in-depth review of existing bubble detection methods, the novel phase detection method was developed to address the shortcomings of the other published methods by more fully utilizing the three-dimensional capability of the sensors. After the sensor parameters were optimized to verify capability of bubble detection, measurements were made with glass beads and quartz sand. A range of air velocities in a 10 cm diameter bubbling fluidized bed were used. The results largely agree with the fundamentals of bubbling fluidization and results from publications with similar experimental setups. Within each measurement the bubble dimensions, velocities and frequencies over the axial and radial position could be evaluated. Due to the three-dimensional nature of the novel bubble detection technique, insight into the directional tendencies of detected bubbles was gained. For example, bubble migration toward the radial center of the bed, radial and axial bubble coalescence, and splitting are more evident from the trends that are producible with this method.

1. Introduction

Detailed knowledge of the dimensions and velocities of bubbles in fluidized beds is invaluable for the development and validation of correlations and models of particles in fluidized bed systems. There are various experimental techniques for non-invasive measurement of bubbles in fluidized beds, like particle image velocimetry (PIV) and X-ray fluoroscopy, which work by taking series of two-dimensional images [1–4]. In both cases, very limited information about the three-dimensional shape of bubbles can be obtained. As such, information about the behavior of bubbles at the wall zone is the primary outcome of experiments using these techniques. Furthermore, for PIV experiments, rectangular pseudo-2D fluidized beds plants with large width-to-depth ratios are often used to increase the visibility of the bubbles. This further increases the effect of the wall zone on the particle flow. More complex methods like positron emission particle tracking (PEPT) [5], magnetic resonance imaging (MRI), radioactive particle tracking (RPT) or X-ray tomography can give a three-dimensional image of a fluidized bed, but these costly systems cannot be universally used with every particle type [6].

Electrical capacitance measurements were used in this study to determine the solid fractions within the fluidized beds. The working principle of this measurement method is the change in the dielectric constant due to the change of solid concentration in an electric field between two electrodes. Electrical capacitance tomography (ECT) involves the use of multiple pairs of electrodes typically arranged in a circular configuration on the exterior of the fluidized bed. By alternating which electrodes are paired throughout the measurement time, tomograms (two-dimensional images) can be developed. These provide a simpler, non-invasive method of identifying areas of low and high solids concentration in fluidized beds. By using only the tomograms from ECT, dimensions and velocities of rising bubbles in bubbling fluidized beds (BFBs) can be measured. However, by implementing ECT in multiple layers, three-dimensional images of rising bubbles can be approximated. This method is known as 3D ECT. The spatial resolution of this method in the axial direction can be increased by also pairing electrodes together such that capacitance plates that span several axial ECT layers are yielded. This method is known as electrical capacitance volume tomography (ECVT). Unlike 3D ECT, ECVT can measure the solids

* Corresponding author.
E-mail address: lennard.lindmueller@tuhh.de (L. Lindmüller).

https://doi.org/10.1016/j.cej.2024.150461
Received 14 November 2023; Received in revised form 22 February 2024; Accepted 14 March 2024
Available online 16 March 2024

Nomenclature

Latin letters

$c_{v,rel}$	relative solid volume fraction (-)
$c'_{v,rel}$	first derivative of relative solid volume fraction (frame^{-1})
D_{bed}	column diameter (cm)
d_b	radial diameter of bubble [17] (cm)
d_{Sauter}	mean Sauter diameter (μm)
H_{bed}	fixed bed height (cm)
h_b	axial bubble length (cm)
h_v	height of voxel (cm)
L_+, L_-	upper/lower fluxion limit (frame^{-1})
L_0	mean temporal volume fraction (-)
L'_0	mean temporal value of $c'_{v,rel}$ (frame^{-1})
n	number of dense phases and dilute phases (-)
t	time (s)
U_g	superficial fluidization air velocity (cm/s)
U_{mf}	minimum fluidization velocity (cm/s)
u_{bubble}	bubble rise velocity (cm/s)

Greek letters

ε_{bed}	bed porosity (-)
σ	standard deviation of temporal volume fraction (-)
σ′	standard deviation of $c'_{v,rel}$ (frame^{-1})
ρ_B	bulk density (g/cm^3)
ρ_S	particle density (g/cm^3)
ω	emulsion phase width in multiples of σ (-)
ω′	emulsion phase width in multiples of σ′ (-)
Ψ_{Wa}	sphericity (-)

Indices

0	mean-phase (emulsion phase)
f	frame (frame number)
rel	relative

Abbreviations

3D ECT	three-dimensional electrical capacitance tomography
3D NN-MOIRT	3D neural network MOIRT
BFB	bubbling fluidized bed
ECT	electrical capacitance tomography
ECVT	electrical capacitance volume tomography
LBP	linear back projection
MOIRT	multicriterion optimization image reconstruction technique
MRI	magnetic resonance imaging
PIV	particle image velocimetry
PoI	distinct mass unit of phase of interest
XRF	X-ray fluoroscopy

concentrations at several axial positions exceeding the number of electrode plate layers without the need for interpolation. This results in increased spatial resolution, which can be very useful in the detection and dimensioning of phases of interest, such as bubbles [7,8].

For ECT and ECVT, the capacitance measurements can be reconstructed into images via several methods. For each pair of source and detector electrodes, the measured capacitance can be expressed via integration of the Poisson equation [9]. This equation directly shows the dependency of the measured capacitance on the permittivity of the substances within the sensor, which is inversely proportional to the dielectric constant. Therefore, by solving for the permittivity distributions, the solid volume fraction distributions can also be calculated. The most effective way of solving this equation for the permittivity distribution is with linearization techniques [7]. Unlike analytical or numerical methods, the linearization techniques result in smooth reconstructed images on the boundaries of sharp objects. However, this effect can be mitigated with increased iteration.

Common methods for image reconstruction are linear back projection (LBP) [10], Landweber (or iterative LBP) [11], and multicriterion optimization image reconstruction technique (MOIRT) [12]. All of these methods use the same general linearization technique, the sensitivity model [7]. In this technique, the volume enclosed by the ECT or ECVT sensor is subdivided into volume elements known as voxels. With changes in permittivity within single voxels, the response of the sensor changes accordingly. The sum of the responses from each voxel and every combination of electrodes is used to solve for the permittivity within each voxel. The global MOIRT objective function is most commonly solved via the Hopfield neural network model [13], yielding the 3D NN-MOIRT technique, introduced by Warsito et al. [7]. The method will be used in this study and is recommended for measurement with room temperature air and particles similar in density and size.

The focus of this study is the development of an improved method for detecting and measuring the size and velocity of phases of interest, like bubbles or slugs, in fluidized beds. The novel bubble detection method was developed to build off of the successes of studies from recent bubble sizing and velocity publications, while also addressing some of the perceived shortcomings of their applied methods. The various methods for bubble detection and velocity-measuring, reported in literature, as well as those developed in this work, are outlined in the following sections. These include nomenclature proposals for the different approaches. Portions of the following explanation of bubble detection and rise velocity methods are also applicable to measurements made with any tomographic technique that generates three-dimensional data, such as MRI. The bubble detection method is then used for experiments with glass beads and quartz sand for three gas velocities, to evaluate the solid volume fraction, radial diameter, axial length, residence time, rise velocity and frequency of bubbles in fluidized beds.

2. Phase detection methods

Several different phases can be defined for a given fluidized bed under a given set of parameters. For gas–solid fluidized beds, the simplest phases to define are the gas phase (e.g., air) and solid phase (particles). Dependent upon the operational parameters being used or the physical phenomena being studied, however, it may be more beneficial to define different phases that exist between these two. By attributing observed fluidization behavior of distinct units of mass within a fluidized bed to their assigned phases, correlations between said behavior, operational parameters, particle-gas-wall interactions, and unit operation designs can be more easily developed. Several bubble tracking methods have been published and used. Due to the lack of unified terminology amongst the relevant literature, Table 1 has been developed to categorize the methods found in literature and the ones developed in this study based on their relationship to time (t), radial position (x & y), axial position (z), bubble diameter ($d_{b,rad}$), and solid volume fraction from the previous frame ($c_{v,n-1}$).

The two main bubble detection categories are the thresholding methods and the fluxion methods. The thresholding methods define limits for the solid volume fraction beneath which a bubble is defined, while the fluxion methods set limits on the rate of change of the solid volume fraction. The thresholding methods are split into the invariant and variant categories. In the former category, the solid volume fraction thresholds are global. They do not change with respect to any of the variables shown in Table 1. While the invariant methods are used by

Table 1
Comparison of bubble detection methods with respect to direct (D) and indirect (I) relationships to the measurement variables, t : time, z : axial position, r : radial position as a function of the position on the x-axis (x) and y-axis (y), $d_{b,rad}$: measured radial bubble diameter, and $c_{v,n-1}$: the solid volume fraction from the previous frame.

Volume fraction bubble detection method				Relationship to:							Sources
				t	z	r	x	y	$d_{b,rad}$	$c_{v,n-1}$	
Threshold	Invariant			-	-	-	-	-	-	-	various [2,4,14–16]
	Variant	Axial	non-iterative	-	D	-	-	-	-	-	none
			iterative	I	I	–	–	–	D	–	Agrawal [17]
		Radial		–	–	D	I	I	–	–	none
		2D		–	D	D	I	I	–	–	none
		3D		–	D	I	D	I	–	–	none
Fluxion		Axial		I	D	–	–	–	–	D	none
		3D		I	D	I	D	D	–	D	current study

many groups, very few variant methods have been developed. As such, the methods without any sources listed exist only in theory. However, Agrawal, et al. [17] successfully implemented the iterative axial threshold method. Therefore, this method is explained in more detail in the following sections. The invariant thresholds have various direct and indirect relationships to the variables listed in Table 1. All of these, however, are not discussed in detail within this work.

The 3D fluxion method was developed in this work to build off of the proven success of the iterative axial threshold method and the hypothesized potential of the entire variant group of thresholding methods. It is the only of all the listed methods that is directly dependent on four different variables, those being the solid volume fraction values from the previous frame and the x–, y–, and z–position. A review of the defining characteristics of the most relevant methods from Table 1 is given in the following sections.

2.1. Invariant threshold method

By far, the invariant threshold method is the most commonly employed method in the literature [2,4,14–16]. With this method, a lower limit for bubbles is defined for the solid volume fraction. For any given measurement, regardless of the position within the fluidized bed, if the limit is exceeded, the distinct unit of material within the measurement volume is defined as a cluster or a bubble, respectively. If the limit is not exceeded, that material is defined as emulsion phase (alternatives: bulk phase or mean phase). Although this method yields thresholds that are invariant with respect to the variables listed in Table 1, the values for the thresholds can vary with respect to experimental conditions, such as the type and mass of particles used and the properties and flowrate of the fluidization gas.

The values for these thresholds can come from literature for similar gas–solid systems, or they can be determined by measuring the mean and standard deviation of the solid volume fraction over a period of time. To calculate these upper and lower thresholds for any number of defined phases, the following equations can be used:

$$L_{+n} = L_0 + \frac{\sigma\omega n}{2} \tag{1}$$

$$L_{-n} = L_0 - \frac{\sigma\omega n}{2} \tag{2}$$

with L_0 being the mean temporal solid volume fraction, σ the standard deviation of the temporal solid volume fraction, ω the width of the emulsion phase in multiples of σ, and n the number of dense phases and dilute phases.

2.2. Iterative axial threshold method

Unlike the invariant threshold methods, the thresholds used with the variant methods can be directly dependent on the positions of the measurements or the measured size of the bubbles. The addition of the location dependencies to the threshold calculations may help to account for differing phase compositions as a function of physical position. It may also aid in dampening any loss of accuracy due to position within the sensor [7]. Studies with invariant threshold methods have failed to identify smaller bubbles, which leads to inaccuracies in bubble size estimation, but Agrawal, et al. [17] developed a method that accounts for this by calculating a solid volume fraction threshold for bubble detection for each measured axial position within the sensor. A method such as this would be labelled a non-iterative axial threshold method, which results in varying solid volume fraction thresholds across the axial length of the sensor. However, the Agrawal group chose to not only account for axial differences in solid volume threshold, but also to vary the threshold based on the measured size of the bubbles. This led to an iterative axial thresholding method, in which the threshold values differed from one measurement frame to the next as a function of measured bubble size.

The Agrawal iterative axial threshold method is based on the development of optimum threshold equations via the repeated measurement of glass beakers with known diameters. Beakers of four different diameters were partially submerged into the bed of sand particles. The beakers were inserted individually and left stationary until a measurement with the ECVT sensor had been taken. Measurements were taken with the beakers placed at several different axial and radial positions. The solid volume fraction results were then used to determine the diameters of the beakers at the different locations. For this step, threshold values were required to designate each voxel as being filled with either sand particles or the empty beaker. By repeating this beaker size measurement with a range of threshold values, the optimum threshold value for each beaker size used was determined. These optimum values were the ones that led to measured beaker sizes that differed from the actual beaker diameters by the least amount. By using a polynomial fit, an equation for the optimum threshold value as a function of beaker size was obtained. The result from the fitted data is shown in Equation (3), where ε_s is the averaged optimum threshold and d_b the bubble diameter:

$$\varepsilon_s = 0.0054d_b^2 - 0.0755d_b + 0.5829 \tag{3}$$

This equation was then used as an approximation for the radial diameter of the measured bubbles. Although the exact amount by which the glass beaker affects the ECVT measurement is not known, the equation was still used in the algorithm shown in Fig. 1 to iteratively adjust the solid volume fraction thresholds for each axial position and measurement frame [17]. Via this algorithm, the optimum solid volume fraction thresholds and bubble diameters are iteratively solved for. For each axial position within the sensor, an initial guess is made for the optimum threshold value. Using this threshold, the bubble diameter is calculated with two different methods. The first method uses the solid volume fraction data from the ECVT measurement. The second method simply

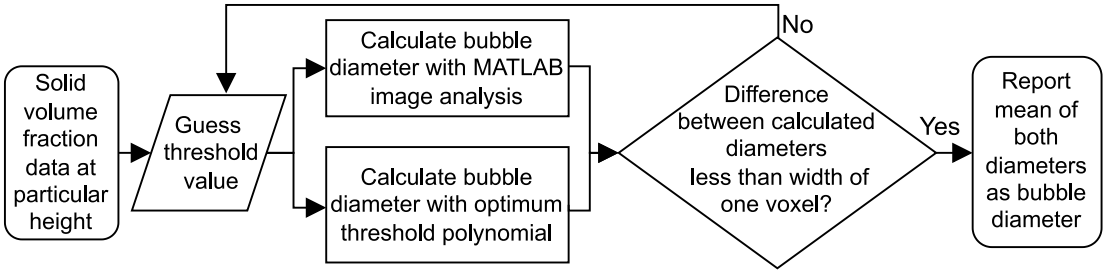

Fig. 1. Bubble diameter algorithm of iterative axial phase-thresholding method (modification from [17]).

back-calculates the bubble size that corresponds to the threshold used via the beaker-fit equation. The bubble diameters obtained via these two methods are then compared to each other. If they differ by more than the width of a single voxel, then a new threshold value is used, and the diameters are recalculated. This iteration continues until the diameters differ by no more than the width of a single voxel, at which point the mean of the two diameters is reported as the width of the bubble at that axial position. This same procedure is carried out for every measured axial position and frame. This results in solid volume fraction thresholds that vary not only from one axial position to the next, but also from one frame to the next. Due to the iterative algorithm converging at a single solid volume fraction threshold value per frame, it is not possible for this method to simultaneously detect two bubbles at the same axial position.

2.3. Three-dimensional fluxion method

As part of this study, a new method for phase detection was developed. The original intention was to use the 3D threshold method described in Table 1. However, as will be shown in this section, there are several potential benefits of using a fluxion limit method instead of a threshold method. Unlike the standard phase threshold methods, the 3D fluxion method does not rely simply on the solid volume fraction for the development of the phase thresholds. The 3D fluxion bubble detection method relies on the rate of change in the solid volume fraction from frame to frame. The first and second derivatives, or fluxions, of the relative solid volume fractions are used to develop detection limits. By doing so, this method allows for more general application of the developed phase limits. This method may allow for the same algorithm parameters to be applied to datasets acquired from experiments with a range of different operational parameters as well as across different raw material systems. Another potential advantage of using the 3D fluxion detection method is its potential to be also used for detection of particle clusters in a riser of a circulating fluidized bed. Fig. 2 shows the solid volume fraction trend for a single voxel during a bubbling fluidized bed experiment. Examples of the dense and dilute phase thresholds, L_{+1} and L_{-1} are shown by the orange lines. These limits are calculated via Equations (1) and (2).

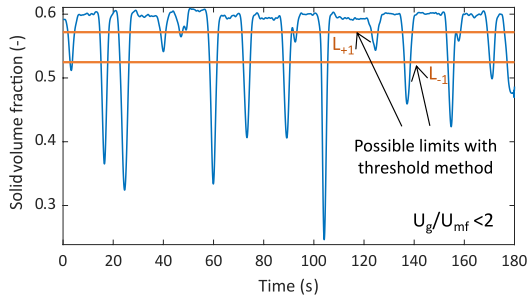

Fig. 2. Temporal solid volume fraction for single voxel with examples of phase thresholds for 180 s measurement.

This fluidized bed was operated under slugging conditions, which resulted in relatively long times between each of the major drops in relative solid volume fraction. As such, the use of Equation (2) results in only eleven bubbles being detected. Furthermore, these detected bubbles are air gaps due to slugging. However, because the mean value, L_0, is greatly affected by the major drops caused by the slugging behavior, the bubble phase threshold, L_{-1}, is set much too low to allow for normal, smaller bubbles to be detected. By taking the first derivative of the relative solid volume fraction with respect to the frame number (or time) via Equation (4), the distribution is transformed into a Gaussian distribution of the adjusted dataset:

$$c'_{v,rel_i} = \frac{c_{v,rel_{i+1}} - c_{v,rel_i}}{n_{f,t_{i+1}} - n_{f,t_i}} \tag{4}$$

with $c'_{v,rel}$ as the first derivative of the relative solid volume fraction, $c_{v,rel}$ the relative solid volume fraction and $n_{f,t}$ the frame number. A standard Gaussian distribution is now a much better approximation of the data, thereby justifying the use of the standard deviation. Eqs. (1) and (2) can now be modified for the calculation of fluxion limits rather than phase thresholds, as shown in Eqs. (5) and (6):

$$L_+ = L'_0 + \frac{\sigma'\omega'}{2} \tag{5}$$

$$L_- = L'_0 - \frac{\sigma'\omega'}{2} \tag{6}$$

with L'_0 being the mean temporal value of the derivative of the solid volume fraction, σ' the standard deviation of that derivative value, and ω' the width of the emulsion phase in multiples of σ'.

A relatively high positive value for the first derivative corresponds to frames in which the bubble is exiting the voxel, since this would result in a rapid increase in the solid content within that voxel. Likewise, a relatively low negative value corresponds to frames in which a bubble is entering the voxel. If the derivative of relative solid volume fraction of the voxel is between L_- and L_+, then the voxel is occupied by either emulsion phase or a bubble that has not yet started to exit the voxel.

Fig. 3 shows a closer perspective of the bubble from Fig. 2, which was detected just before 80 s. Also plotted on this figure are the first and second derivatives, $c'_{v,rel}$ and $c''_{v,rel}$, which have been scaled up from a mean value of zero to one for visualization purposes. The bubble exit and bubble entry limits, L_+ and L_- define the bubble boundaries. From 65 s to 71 s, this voxel was occupied only by the emulsion phase. The relative solid volume fraction changed from frame to frame, but not by so much that the bubble entry limit was exceeded. Around 71 s, this limit was exceeded. This triggered the "steep decline" portion of the algorithm. Until the remaining four conditions A, B, C, and D were sequentially met, this voxel was designated as containing only bubble phase. As the bubble continued to enter the voxel, the relative solid volume fraction dropped until it reached a minimum value at around 73 s. At this point, when the first derivative switched from negative to positive, the "incline starts" portion of the algorithm was triggered. This

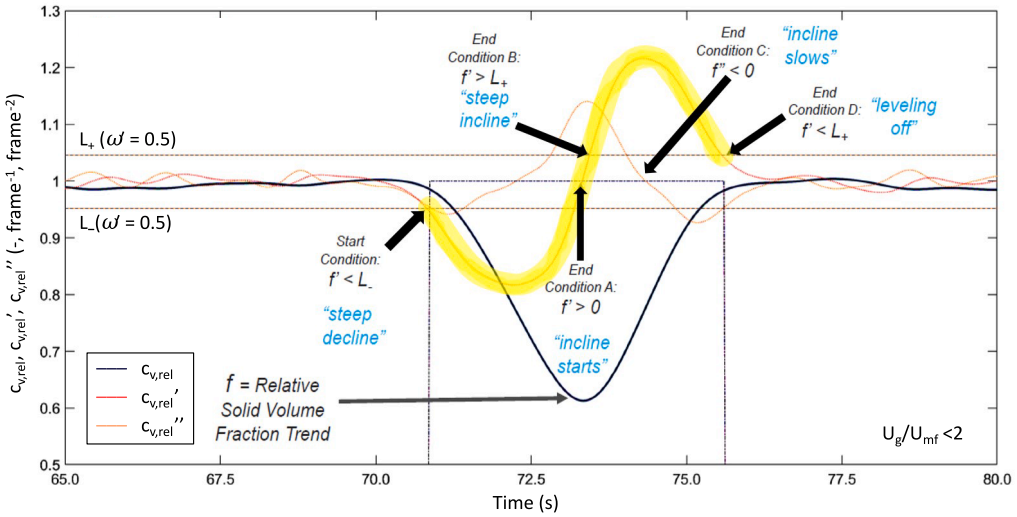

Fig. 3. Fluxion trends of detected bubble with labelled algorithm triggers and steps. The relative solid volume fraction, $c_{v,rel}$, its first and second derivatives, and the fluxion limits are plotted for a 180 s measurement with $\omega' = 0.5$.

Table 2
Comparison of bubble rise velocity methods. The methods are compared based on their relation to bubble definitions, radial velocity component, and bubble-surface velocity profiles.

Method	Utilizes existing bubble definition?	Radial velocity component?	Velocity profile across bubble surface?	Study
Minimum solid volume fraction	NO	NO	NO	Agrawal et al. 2018 [17]
Maximum bubble diameter	YES	NO	NO	McKeen & Pugsley 2003 [1]
Centroid-tracking method	YES	YES	NO	Weber & Mei 2013 [16]
Direct axial method	YES	NO	YES	current study

is the point at which the bubble started to exit the voxel. Shortly after, the second condition for bubble exit was met when the first derivative exceeded the bubble exit limit, L_+. This triggered the "steep incline" portion of the algorithm. This incline in the relative solid volume fraction continued for another short time before it started slowing down. This resulted in the second derivative going from a positive to a negative value, which triggered the "incline slows" portion of the algorithm. Whenever the first derivative of the relative solid volume fraction dropped back below the bubble exit limit, L_+, the bubble was considered to have completely exited the voxel. This triggered the "leveling off" portion of the algorithm, which caused all successive frames for this voxel to be designated as containing emulsion phase. The yellow highlighted S-curve of the derivative with a start and end just outside of the bubble entry and exit limits is a defining characteristic for any detected bubbles.

In summary, the steps of a bubble rising through a voxel are listed below with descriptions of the respective algorithm triggers that are also shown in Fig. 3:

(1) Bubble detected: $c'_{v,rel} < L_-$
(2) Bubble "peak": $c'_{v,rel} > 0$
(3) Steep incline: $c'_{v,rel} > L_+$
(4) Incline slows: $c''_{v,rel} < 0$
(5) Leveling off: $c'_{v,rel} < L_+$

3. Bubble rise velocity detection methods

There are several methods that are commonly used to estimate the rise velocity of bubbles. A summary of these methods is shown in Table 2. The first of the three groups of these methods are the time series methods. This group of methods is the only one that has been completely utilized for bubble rise velocity estimation in literature. Unlike the centroid-tracking and direct axial groups of methods, the time series methods can sometimes use completely different bubble definitions for bubble sizing and bubble velocity estimation. This creates a lack of uniformity in the resulting data. The centroid-tracking method not only accounts for this, but it also allows for the determination of radial velocity components. The method developed in this study, the direct axial method, does not easily allow for the calculation of these radial components, but it does allow for the measurement of the rise velocity at multiple spots on the upper and lower surfaces of the bubbles. In the following sections, the steps required for each of these methods are explained in greater detail.

3.1. Time series bubble rise velocity methods

The time series group of rise velocity methods includes all methods that use the minima and maxima of one or more temporal trends to estimate the rise velocities of bubbles. These methods require the correlation of these trends at two different axial positions with known vertical separation. By estimating the amount of time that passes between two correlated events at these axial positions, the velocity of the bubbles rising between these two axial positions can be estimated. Since this group of methods only requires measurements at two positions, it can also be used with one-dimensional capacitance probes [18] or fiber optic probes [19], which makes validation measurements for these methods especially simple.

3.1.1. Minimum solid volume fraction bubble rise velocity method

The first time series method does not require the bubbles to have been previously identified. Although not found in the literature, this could even allow this method to take the place of a phase thresholding method for bubble detection. The method requires the solid volume

fraction at two different axial positions to be measured over time. These trends could originate from single points from a one-dimensional capacitance probe, from individual voxels within an ECVT sensor, or from radially averaged data from an ECT cross-section. Of prime importance is only that the distance between the two axial positions is known and that the bubbles being measured are present and measurable at these two positions. Due to the latter point, great distances between the two axial positions may yield erroneous results. Furthermore, using cross-sectionally averaged data from fluidized beds with large diameters may lead to bubbles not being detected. The Agrawal group used cross-sectionally-averaged data for their measurements with a 20 cm diameter fluidized bed [17].

3.1.2. Maximum bubble diameter bubble rise velocity method

The other common time series method is the maximum bubble diameter method [1]. This method requires the rising bubbles to have already been detected and measured. This gives this method the advantage of not having multiple definitions for each phase. All frame-voxel combinations have already been designated as emulsion- or bubble-containing. Whereas the minimum volume fraction method used an approximation for the maximum radial bubble diameter at two different axial positions, the maximum bubble diameter method measures this diameter at these two positions. This eliminates the possibility of using one-dimensional capacitance probes with the measurement technique. However, this allows for the use of multiple pairs of planes to track the change in bubble rise velocity as a function of axial position.

3.2. Centroid-tracking bubble rise velocity method

Another method to calculate bubble rise velocity involves the tracking of bubbles' approximated centers of gravity in three dimensions over time. Weber and Mei [16] used centroids in bubbling fluidized beds to yield information about the shape of rising bubbles. The invariant thresholding method was first used to determine which voxels were occupied by bubbles. The center of mass of each bubble was then calculated under the assumption that every voxel occupied by a bubble was filled with the same mass of air and particles in dilute phase. By storing the xyz-coordinate values of the centroid of each bubble from frame to frame, the approximate location of each bubble can be tracked over time. This would not only allow for the additional calculation of the radial components of bubble velocity, but it would also allow for simple estimation of bubble acceleration. However, this method, just like the ones before, does not allow for the bubble rise velocity to be measured at multiple points along the bubbles' upper or lower surfaces.

3.3. Direct axial bubble rise velocity method

$$u_{bubble} = \frac{\Delta h}{t_R} = \frac{h_b - h_v}{t_3 - t_2} \tag{7}$$

The direct axial method was implemented in this study. This method, like the centroid-tracking method, requires the bubbles to have already been identified. Additionally, the axial lengths of the bubbles must have already been calculated for this method. Fig. 4 shows a visual representation of a bubble rising through a voxel. The bubble and voxel have both been condensed to two-dimensional rectangles for clarity. Furthermore, the bubble is represented by a cube of invariant dimension rather than as a spheroid or other more realistic shape with varying dimensions from frame to frame. As the bubble rises vertically into and through the voxel, there is a period of time in which the voxel is completely filled with the bubble. This time is known as the residence time t_R, and equals the time difference between frames 2 and 3 in the figure. By dividing the difference between the axial length of the bubble and the known height of a voxel by the residence time, the bubble rise velocity can be calculated with Equation (7):

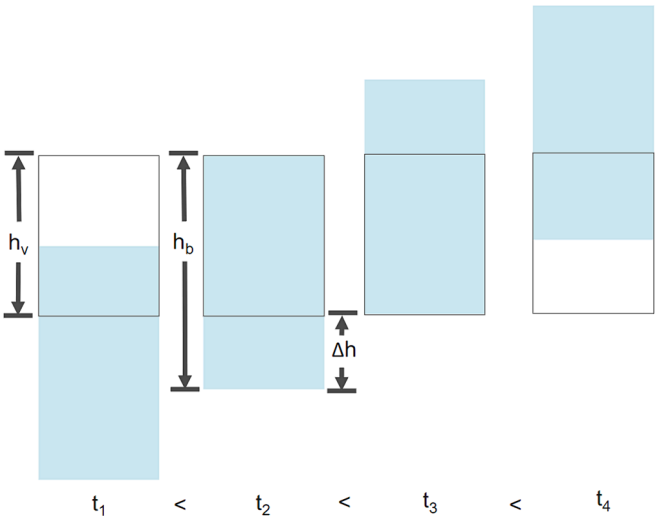

Fig. 4. Ideal bubble rising through single voxel for four measurement times. The residence time is the amount of time that the voxel is filled with the bubble (h_v = height of the voxel, h_b = height of the bubble).

4. Experimental setting and methods

4.1. Experimental equipment

The fluidized bed reactor consists of acrylic gas with an inner diameter of 10 cm and a height of 1 m, with a porous plate gas distributor. The facility is fluidized with pressurized air, which is controlled with a rotameter. The fixed bed height was 30 cm. The ECVT sensor was mounted 6 cm above the gas distributor. A picture of the lower part of the facility with the ECVT sensor is shown in Fig. 5.

The measuring system consists of an ECVT sensor, Model *4RD Cold Flow* by *Tech4Imaging* with 24 electrodes (divided into four axial levels) and the accompanying data acquisition system. The sensor has a height of 215 mm and an inner diameter of 110 mm. The sensor has a spatial resolution of 20 × 20 × 20 voxels. The measuring range has a diameter of 110 mm and a height of 224 mm, meaning that each of the 8000 voxels measures 5.5 mm × 5.5 mm × 11 mm (length, width, height). This results in a voxel volume of 0.333 cm^3. The excitation frequency can be adjusted between 62.5 kHz and 8000 kHz. The sensor housing is composed of printed plastic filament and is coated with electrically conductive nickel paint [20]. It is well known that ECVT is a soft–field technique, meaning that the magnitude, accuracy, and

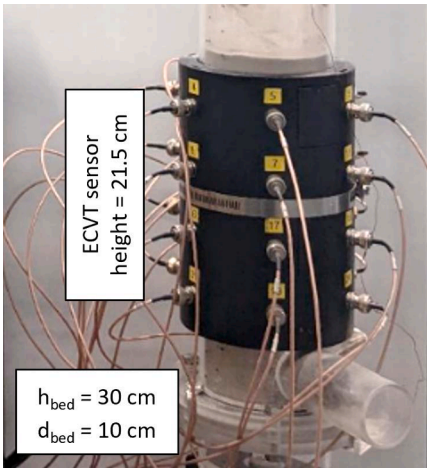

Fig. 5. Picture of lower part BFB plant with mounted ECVT sensor, 6 cm above gas distributor.

precision of measurements can differ greatly depending on the exact spot within the sensor region at which the measurement is taken [17]. For example, due to the decreased number of voxels and the increased distance from electrode plates, the accuracy and precision of measurements taken at the radial center of the ECVT sensor is lower than it is at the wall zone [7]. Furthermore, some trends developed in the current study could also serve as evidence for measurement accuracy being partly dependent on axial position within the sensor as described in section 5.2. Overcoming this source of error is the primary objective behind both the iterative nature of the bubble thresholding method developed by Agrawal et al. [17] and the time-dependent nature of the fluxion bubble detection methods developed in the current study.

Two different bed materials were used in this study. Quartz sand and glass beads are extensively used Geldart B particles and serve as reference for spheric and coarse particles. Images of the particles taken with a microscope are shown in Fig. 6. The particle characterization including the particle size distribution, particle sphericity, bulk density, particle density, and minimum fluidization velocity, is shown in Table 3. The cumulative (Q_3) distribution from the particle size distribution analysis for the particles is plotted in Fig. 7.

4.2. Measurement parameters

The ECVT sensor excitation frequency, f_{exc}, is the electrical frequency at which the electrodes in the capacitance plates operate. The available excitation frequencies range from 62.5 kHz to 8 MHz. After some preliminary experiments with quartz sand, the measurements obtained with a 1 MHz excitation frequency were found to be the most distinguishable from one another. Thus, 1 MHz was chosen as the ECVT excitation frequency for the remainder of the measurements. Regarding the measurement time, Makkawi et al. [21,22] recommend using a measurement time of at least 10–80 s, depending on the number of phases measured. For increased measurement accuracy and statistically meaningful fluxion limits (section 2.3), a measurement time of 180 s was used for all experiments in this study, far surpassing the recommendations from literature. In all presented results, the temporal average across this timeframe will be used. For all experiments, three gas velocities were investigated: 8, 12 and 16 cm/s. This resulted in U_g/U_{mf} ratios of 1.1, 1.7, and 2.3 for glass beads and 2.1, 3.2, and 4.2 for quartz sand, respectively. The results are represented as radial and axial plots. Radially, all voxels with the same distance from the center are summarized at each respective radial position, which results in 35 data points from the given 20x20 X-Y coordinate grid. Since 20 voxels are generated along the Z-axis, 20 data points are used axially. The error bars in the plots represent the standard deviation between the values for these different voxels, but not the standard deviation between the temporal values.

4.3. Reconstruction algorithm and parameters

For the image reconstruction, the *MATLAB* script provided by *Tech4Imaging* was used. The image reconstruction generates 4D arrays (x-axis, y-axis, z-axis, and time) of the solid concentration from the measured data. As mentioned in the introduction the 3D NN-MOIRT technique introduced by Warsito et al. [7,13]. was used in this study. Two parameters within this script can be altered to increase the performance of the image reconstruction. The first is the number of iterations, n_{iter}. This is simply the number of iterations the script is allowed for the convergence solution of the inverse image problem. By increasing the number of iterations, the images yielded become more accurate, but the evaluation time is increased. A value of 300 iterations was chosen for this study. The other parameter in the image reconstruction script is the alpha value, $\breve{\sigma}$. This value affects the sharpness of the reconstructed images. For measurements with disperse boundaries, such as bubbles, the manufacturer recommends a low value near 15. Hence, a value of 15 was used for all measurements in this study. The reconstructed measurement data is then fed into the scripts for phase analysis.

In the 3D fluxion phase detection script, a mean fluxion phase width ω', of 0.5 was used for all measurements. As described in section 2.3, a higher ω' would lead to smaller detected bubbles. With this value, acceptable results could be generated. Via comparisons with other tomographic methods, like MRI this parameter can be optimized in the future to match experimental data.

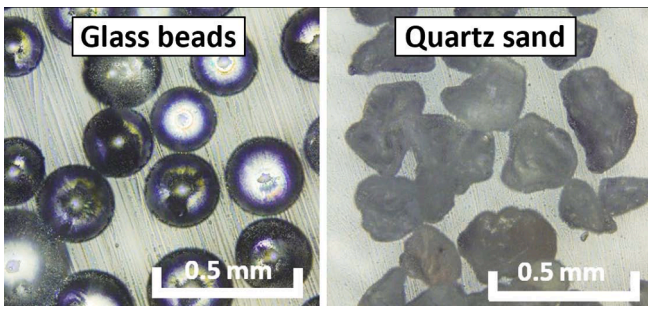

Fig. 6. Glass beads and quartz sand images taken with light microscope at 10x magnification.

Table 3
Properties of the used Geldart B particles glass beads and quartz sand.

Property	Unit	Glass beads	Quartz sand
Sauter mean diameter, d_{Sauter}	μm	263	189
Bulk density, ρ_B	g/cm^3	1.47	1.37
Particle density, ρ_s	g/cm^3	2.49	2.60
Bed voidage fraction, ε_{bed}	–	0.41	0.47
Sphericity, Ψ_{Wa}	–	0.94	0.79
Minimum. fluidization velocity, U_{mf}	cm/s	7.0	3.8

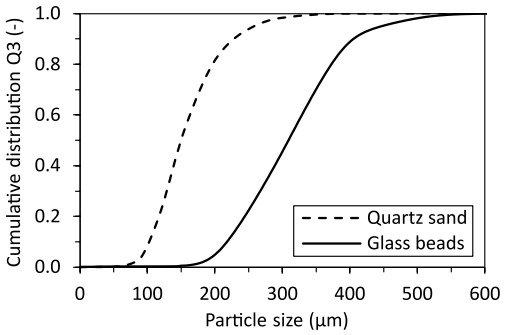

Fig. 7. Cumulative particle size distributions (Q3) of quartz sand and glass beads.

4.4. Scripts for phase analysis

This section is a detailed explanation of the scripts used for phase detection, sizing, and velocity estimation. In the start of this section, an overview of the master script is given. The three subsequent subsections contain more specific details about each of the minor scripts for phase detection, residence time, and dimensioning.

All phase analysis scripts were written in *MATLAB* 2021*a*. An overview of the master script's functionality is shown as a flowchart in Fig. 8. The primary input for the script is the 4D array of solid volume fractions. The values in this array are first smoothed ten times across ten frames (0.06 s) to reduce the effect of measurement noise on the analysis. After the data has been smoothed, the distinct mass units of the Phase of interest (Poi) are detected. For the current study, the only phases of interest are bubbles. As such, for all following figures, Poi refers to individual bubbles. If accurate experimental data is available, the script

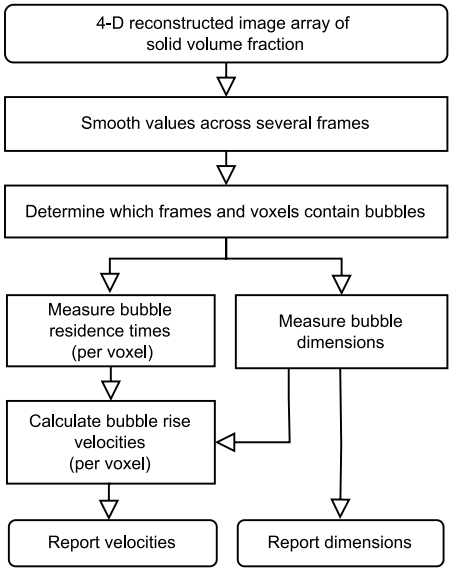

Fig. 8. Flowchart of bubble detection and analysis script.

would also be able to analyze e.g., particle clusters in a circulating fluidized bed. The method used in this study, the 3D fluxion phase detection method, is described in detail in section 2.3. After the algorithm detects the bubbles from one set of data, the residence times and dimensions of each bubble are measured. The dimensions are reported, while the residence times is to calculate the rise velocities of the bubbles with the direct axial method (section 3.3), which are subsequently reported. The script further generates a 4D phase-detected array, which is also used to create the videos and pictures of bubbles rising through the sensor region. The 4D arrays of the dimensions and residence times are used to create 3D, time-averaged arrays, as well as 2D radially- or axially- averaged arrays, all of which are used extensively to produce the figures shown in the results.

4.4.1. *Phase detection script*

The flowchart for the phase detection script is shown in Fig. 9. This script implements the newly developed 3D fluxion phase detection. The smoothed 4D solid volume fraction arrays are the primary input. If cluster detection is desired instead of bubble detection, then these values are first converted from solid volume fractions to gas volume fractions. Following this step, the first and second derivative of these values is calculated for every frame for a single voxel. The upper and lower fluxion detection limits, L_- and L_+, respectively, are then calculated for this voxel with the use of Equations (4). For this step, the width of the emulsion phase, ω', in multiples of the standard deviation of the calculated first derivatives of the measured volume fractions is required. All these derivative values and the limits are required for the algorithm to check for each of the triggers that indicate the steps of bubble progression vertically through a voxel. After the limits have been calculated, each voxel is analyzed frame-by-frame for the presence of bubbles or clusters. As shown in Fig. 3, a bubble entry into a voxel is defined as the frame during which the first derivative of the relative volume fraction drops below the lower fluxion limit, corresponding to a rapid drop in either solid or gas content, respectively. As such, a bubble is first detected by the algorithm when the first derivative is less than the lower limit, L_-.

After the entry of the bubble is detected, the four different steps shown in Fig. 3 must occur sequentially for the exit to be detected. This prevents signal noise from causing the early detection of the exits of bubbles. However, this also eliminates the possibility of distinguishing very small bubbles from one another, since the voxel must be occupied for at least three frames for the exit of the bubble or cluster to be

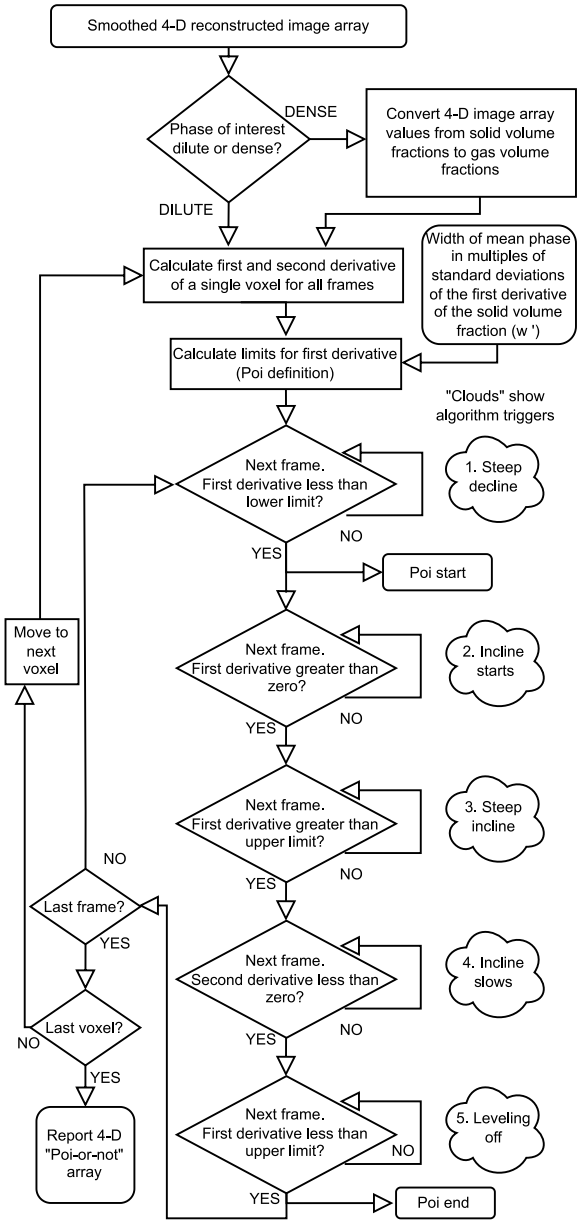

Fig. 9. Flowchart of phase detection script with algorithm triggers from Fig. 3: (Poi = Phase of interest: bubble or cluster).

detected. As such, if the entry of a real bubble that exists within a voxel for fewer than three frames is detected, then its exit will not be detected. The exit of the following bubble will be detected and the two will be treated as a single bubble.

As shown in Fig. 9, the first and second conditions for bubble or cluster exit are triggered whenever the first derivative of the relative volume fraction exceeds zero and the upper fluxion limit, respectively. These occur only once the volume fraction for the voxel starts increasing, indicating the start of the bubble or cluster exit from the voxel. For the second condition to be triggered, this increase must be rapid. The third condition for bubble or cluster exit is triggered whenever this rapid increase starts to slow down, which is indicated by the second derivative of the relative volume fraction decreasing from a positive value to a negative value. This corresponds to a relative maximum in the first derivative trend of the relative volume fraction. Once this derivative drops back beneath the upper fluxion limit, the final condition for bubble or cluster exit is fulfilled. This indicates that the

solid volume fraction is still increasing, but at such a low rate that the voxel is considered to now contain only the emulsion phase. Once these four conditions necessary for exit detection have been fulfilled, the exit is detected, and this process is repeated until all frames have been analyzed. Once all frames have been analyzed, the same process is repeated until all voxels have been analyzed. This results in a 4D array, in which every combination of voxel and frame number has been designated as either bubble phase or emulsion phase.

4.4.2. Residence time script

After the bubbles have been detected, the residence times of each one can be measured. The flowchart for the residence time script is shown in Fig. 10. The 4D array from the phase detection script is the primary input. Starting with the first voxel, the presence of bubbles is monitored on a frame-by-frame basis. Once a frame containing a bubble is found, the frame counter begins. The script then continues monitoring the subsequent frames for this voxel until the emulsion phase is detected again. This triggers the frame counter to stop. The resulting frame count for the bubble is used elsewhere in the script to calculate the residence time of this specific bubble within this voxel. This process is repeated until the final frame has been evaluated. The script then proceeds to the next voxel and the entire process is repeated until all voxels have been evaluated. The resultant 4D array contains the residence times for every bubble or cluster that passed through every voxel.

4.4.3. Dimensioning script

The dimensioning is also based on the 4D array of detected bubbles. The flowchart for this script is shown in Fig. 11. The phase-detected

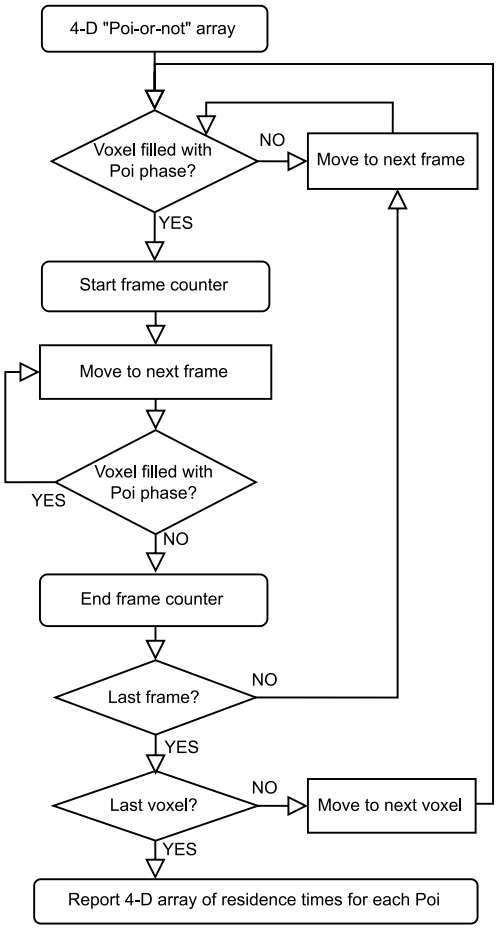

Fig. 10. Flowchart of residence time script (Poi = Phase of interest: bubble or cluster).

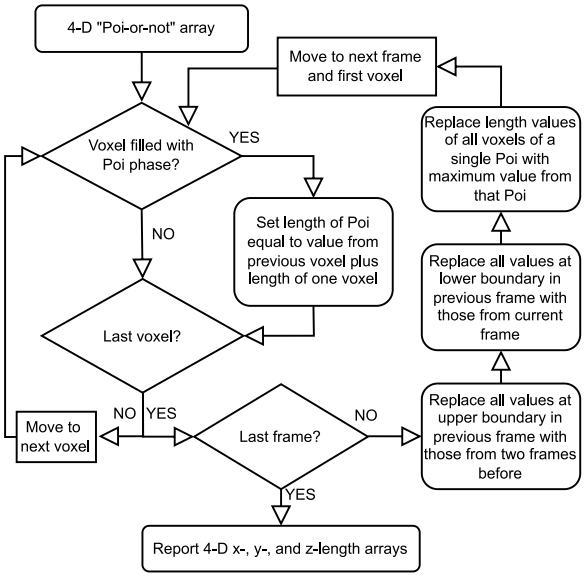

Fig. 11. Flowchart of dimensioning script (Poi = Phase of interest: bubble or cluster).

arrays are analyzed on a voxel-by-voxel basis for a single frame. Starting with the first voxel, the script counts the number of adjacent voxels that are occupied by the phase of interest in the x-, y-, and z-directions. It does so by adding the length of one physical voxel to the length value from the previous voxel, if and only if said voxel contains the phase of interest. If it does not, then the length for that voxel remains zero. This process independently accumulates the measured length along all three axes. Once this has been done for every voxel of a single frame, a few steps must be taken before proceeding to the next frame. First, the length values from the previous frame at the top cross-section of the sensor are replaced by the values from the preceding frame. This helps to prevent the false detection of very small bubbles or clusters at the superior region of the sensor by assuming that their dimensions do not change after rising vertically out of the sensor. A similar correction is then performed for the lower cross-section. Here the length values from the previous frame are replaced by those from the current frame. This also helps to prevent the false detection of very small bubbles or clusters at the inferior region of the sensor by assuming that their dimensions did not change while rising vertically into the sensor. After the values at these two boundaries have been adjusted, the values for the bubble dimensions are rounded up to the maximum values found within that bubble. This step backfills all the lower, intermediate values that were produced during the length accumulation step. After these values have been backfilled, the next frame is analyzed. The entire process is repeated until all frames have been analyzed. This results in three 4D arrays with bubble dimensions, one for each axis (x, y, and z).

5. Results

In this chapter, the experimental results from the 3D fluxion bubble detection and tracking algorithm for the bubbling fluidized bed experiments with glass beads and quartz sand are shown. In the first subsection, a summary of the preliminary work for confirmation of the algorithm functionality is given. This is followed by a detailed discussion of the observed fluidization behavior of the different particles with respect to the ECVT measurements and accompanying bubble detection script results. Where applicable, the results are compared with results from publications with similar experimental setups.

5.1. Validation of algorithm

To confirm the functionality of the developed 3D fluxion bubble detection script, first an initial functionality test was conducted with a hollow plastic ball as a bubble substitute. In a second step, several sets of synthetic data were fed to the script as virtual bubbles with predefined shapes and sizes, which is used to validate of the method.

5.1.1. Bubble substitute

A single hollow ball of 3.4 cm diameter was placed on the distributor plate, as shown in Fig. 12. The pipe was then filled with glass beads up to an axial position five centimeters above the top of the ECVT sensor. After starting the ECVT measurement, the fluidization air was increased to the minimum fluidization velocity of the glass beads, which led to the slow rise of the ball up through the ECVT sensor to the top of the bed.

After image reconstruction, the 3D fluxion bubble detection algorithm was used to identify the ball rising through the bed. Fig. 13 shows three frames of the detected bubble/ball. In this figure, voxels occupied by a detected bubble are colored red with different colored edges to better differentiate between the shapes. Voxels occupied by detected emulsion phase are transparent. In the shown frames, the ball is detected as a single, round bubble. Since the voxels are either defined as emulsion or bubble phase at a specific time point, the data is not perfectly smooth. The presence of the ball in the fluidized bed may have allowed for rising air to flow around the ball by moving against the plastic, which could also explain the non-spheric shape. Furthermore, this test may have also been affected by the difference in permittivity between the air and the material of the ball. Although the plastic ball does not resemble the behavior of an air bubble, the test serves as a functionality confirmation for the 3D fluxion bubble detection algorithm with data from the ECVT sensor. The algorithm is able to detect moving, air filled objects in a fluidized bed from just the rate of change in the solid volume fraction from frame to frame and not simply from the solid volume fraction for the development of the phase thresholds.

5.1.2. Virtual bubbles

As validation step, synthetic data of an ideal fluidized bed with different sized bubbles, depicted as step functions, was fed into the 3D fluxion algorithm. Each voxel occupied by a virtual bubble has a value of zero for the relative solid volume fraction. The emulsion phase around the bubbles was generated by a 20x20x20 voxel matrix, corresponding to the ECVT measurement data with values of one for the relative solid volume fraction, which is the same than a fixed bed. Lower values, which would better represent the bed expansion at a gas velocity just under the minimum fluidization velocity do not change the results, since the algorithm works with the rate of change in the solid volume fraction from frame to frame. Furthermore, several types of random noise at the same magnitude as the variation of a fixed bed measurement were tested. Since the noise does not pass the five conditions in the 3D fluxion algorithm to be designated as bubble phase (see section 2.3) it is not detected as a bubble.

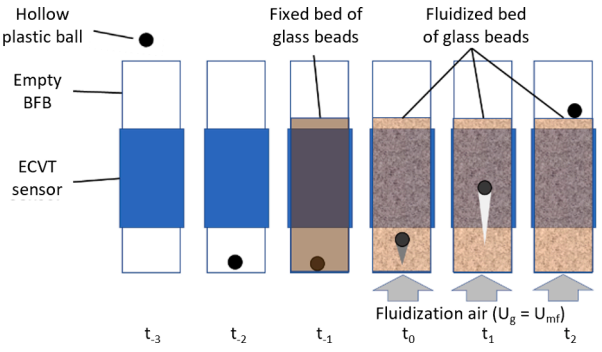

Fig. 12. Rising ball test steps. The plastic ball is placed on the distributor plate before the BFB is filled with glass beads. The ECVT measurement is then started before the fluidization is initiated.

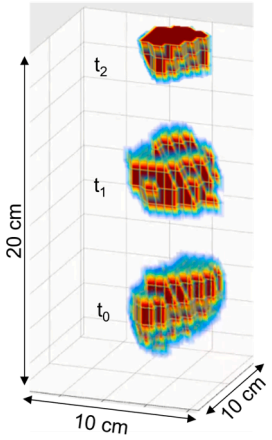

Fig. 13. Rising ball test-bubble detection results. The transparent voxels were not detected as bubbles. All colored voxels were detected as containing a bubble. The color scale is used to better differentiate between the shapes.

As an example, two virtual bubbles with a width of 5x5 voxel (center bubble) and 1x1 voxel (corner bubble) and a height of 4 voxels rose up with a speed of 1.1 cm/s (one voxel per second) until they exited through the top of the sensor region. The 4D matrix of the reconstructed images of the relative solid volume fractions was then fed to the bubble detection algorithm. Fig. 14 shows three frames of what the algorithm detected as bubbles. The detected virtual bubbles are clearly defined, rising from the bottom of the sensor to the top. Exemplarily, the radial bubble diameters plotted over radial position are shown in Fig. 15. The resulting calculated radial bubble diameters match the x and y voxel size of the synthetic data. Additionally, the axial bubble length and bubble rise velocity were calculated correctly. This proves the capability of the algorithm to simultaneously detect multiple bubbles at the same radial position with different sizes. More than ten different cases with virtual bubbles were tested, with either just one bubble, more than five bubbles, different shaped bubbles, or different sized bubbles. Also, a delay between the bubbles entering the virtual measurement region matrix was used. Ultimately, all were detected. If three-dimensional input data has defined differences between the bubble and suspension phase, the phases will be detected by the algorithm.

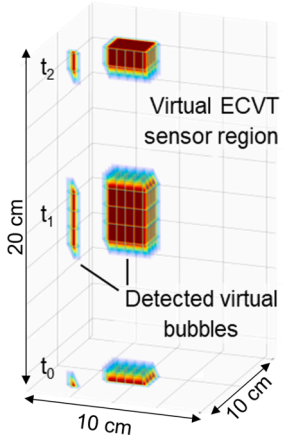

Fig. 14. Two virtual rising bubbles detected with 3D Fluxion script. The transparent voxels were not detected as bubbles. All colored voxels were detected as containing a bubble. The color scale is only for motion visualization.

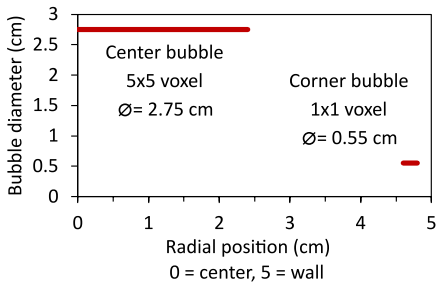

Fig. 15. Radial bubble diameter over radial position of two virtual bubbles.

5.2. Solid volume fraction

As an exemplary result, Fig. 16 shows the solid volume fraction trends for glass beads at U_g/U_{mf} of 1.1 and 2.3 from a 180 s measurement. The plots on the left show the radial dependency of the solid volume fraction for three different axial positions in the fluidized bed. The right column shows the axial trends for three radial positions in the bed: center region (0.4 cm), near the wall (4.0 cm), and between these positions (2.8 cm). The values on the radial trends are not only the temporal mean values, but also the radial mean values for all voxels that are equidistant from the radial center of the column. This results in 35 data points for all shown radial trends from the 20x20 measurement grid at each axial position. As such, the error bars represent the standard deviation between the values for these different voxels, but not the standard deviation between the temporal values.

While the radial and axial trends of the solid volume fraction at U_g/U_{mf} of 1.1 were mostly alike, the trends for U_g/U_{mf} of 2.3 clearly show that the solid volume fraction at the wall is higher than in the center. With increasing axial position, this difference is even higher, which indicates that the bubbles near the distributor are migrating laterally toward the radial center of the column and coalescing with other bubbles along the way. This migration results in an area of low solid content at the wall near the distributor and at the radial center far away from the distributor. This behavior is also confirmed by the axial trends, wherein only the solid volume fraction at the center decreases with increasing axial position.

A comparison of the solid volume fraction of the glass beads and quartz sand is shown in Fig. 17. Unlike the previous figure, the values shown in the radial trends were averaged across all axial positions. Likewise, the values of each axial trend have been averaged across all radial positions. This results in trends that do not fully reveal the movement of the bubbles that was detailed in the previous passage, but it does allow for more intuitive comparison of the bubble properties for different bed materials at different fluidization air velocities. The radial and axial trends of the solid volume fractions now show more clearly that an average axial dependence is nearly non-existent, while the radial dependence grows with increasing fluidization air velocity. Although the general solid volume fraction trends of glass beads and quartz sand are the same, the difference between the values at the radial center and the wall zone is increased for the quartz sand measurements. This is likely primarily due to the lower sphericity of quartz sand, leading to stronger particle–particle and particle–wall forces. The lower average solid volume fractions at the center are due to the increased size of the bubbles, most of which move and coalesce laterally toward the radial center of the column.

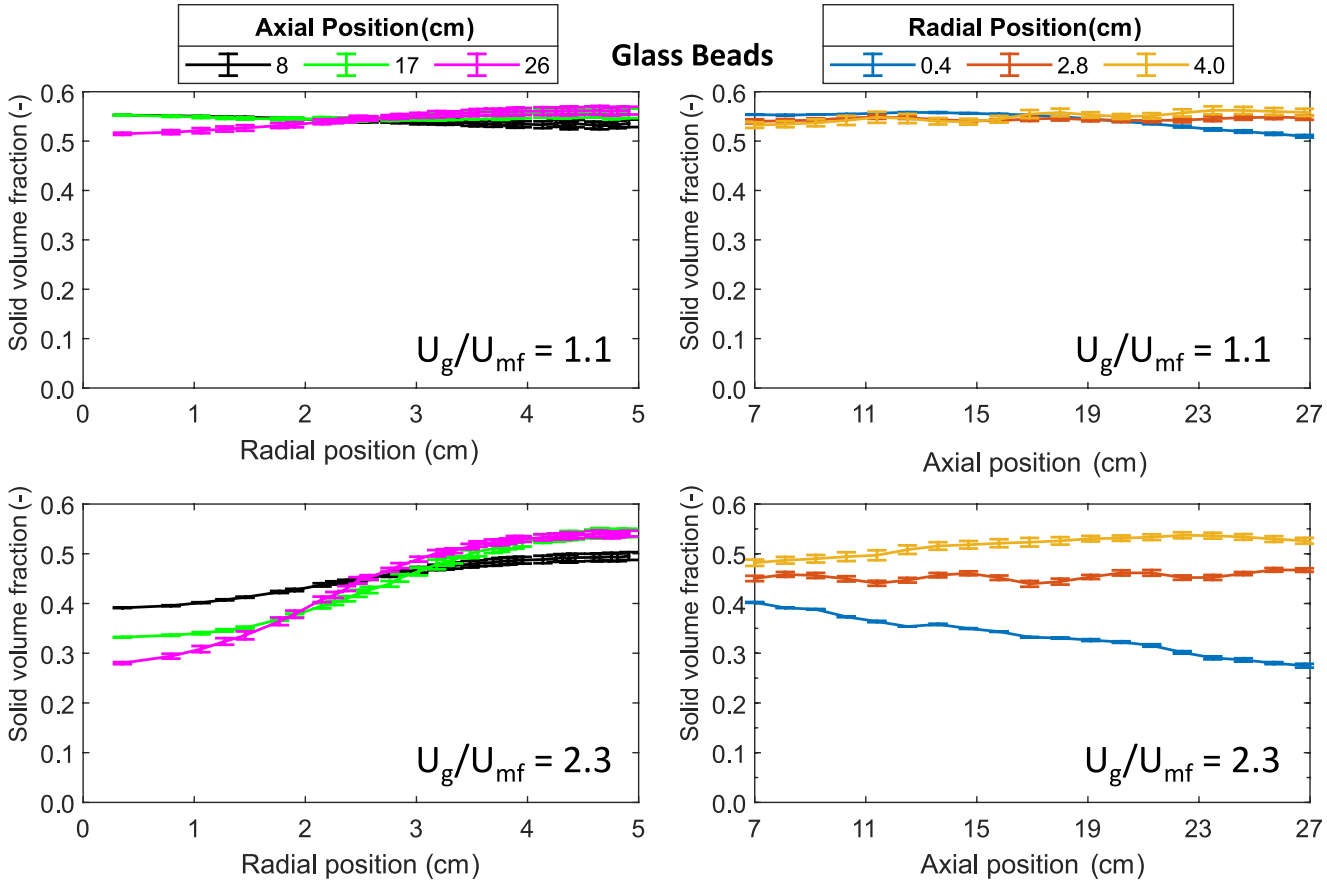

Fig. 16. Radial and axial trends of solid volume fraction of glass beads for U_g/U_{mf} = 1.1 and 2.3. Values were averaged temporally and plotted for three axial positions above the distributor (left) and three radial positions (distance from center of bed) (right).

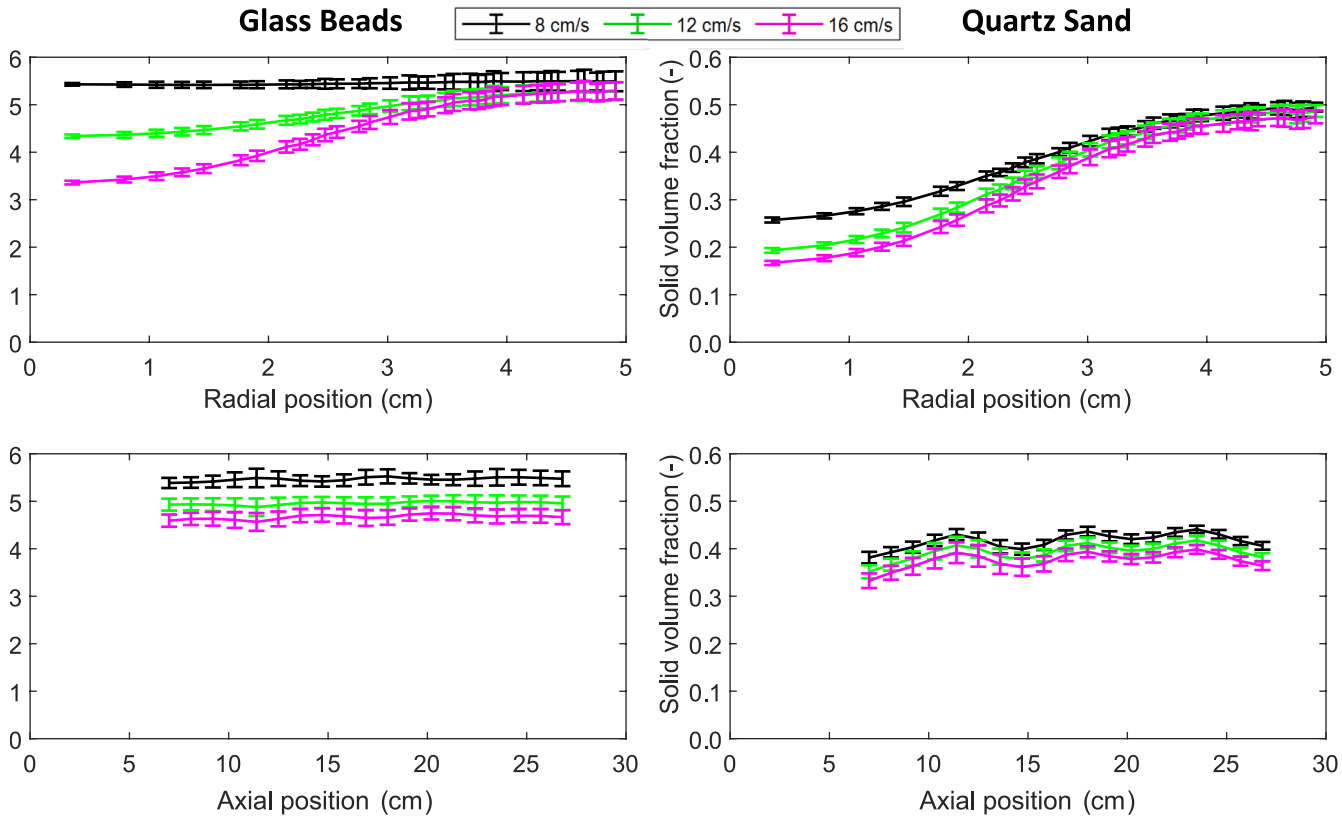

Fig. 17. Radial and axial trends of solid volume fraction for glass beads, quartz sand for three gas velocities.

Among these most similarly shaped solid volume fraction trends, the greatest difference in shape may be a function of sensor sensitivity in the axial direction. This is most noticeable in the quartz sand axial trends of solid volume fraction. Since the solid volume fraction is used for every other calculation of bubble properties, the bubble length, bubble velocity and bubble frequency will show particularly strong dependence on the sensor height. In each of these trends, there exist either four distinct minima or maxima, all occurring at approximate axial positions of 7, 14, 20, and 27 cm. Since these relative extrema are nearly equidistant from each other and span the entire axial length of the ECVT sensor, this is an indication that the measured values are somewhat dependent on the axial positioning of the sensor. The former axial position is nearly level with one of the four rows of electrode plates in the ECVT sensor and the two latter positions are nearly at the axial midpoint of two rows of electrode plates. This indicates that the measured signal is an indirect function of the axial separation from the nearest row of electrode plates. Nevertheless, the trends are still comparable with results from other materials and literature.

The results of this study were compared to the ECVT studies, reported by Agrawal et al. [17] (H = 35 cm, D_{bed} = 20 cm, bed material: quartz sand, d_s = 320 μm, detection method: iterative axial threshold) and by Weber and Mei [16] (H = 26.2 cm, D_{bed} = 10 cm, bed material: glass beads, d_s = 185 μm, detection method: invariant threshold). Fig. 18 shows the relationship between solid volume fraction and dimensionless radius, r/R for glass beds and quartz sand from this work, in comparison to the results of Agrawal et al. [17] and Weber and Mei [16] at two gas velocities each. For a better overview the data points of the comparative works are connected with lines. Fig. 18 does not show error bars due to

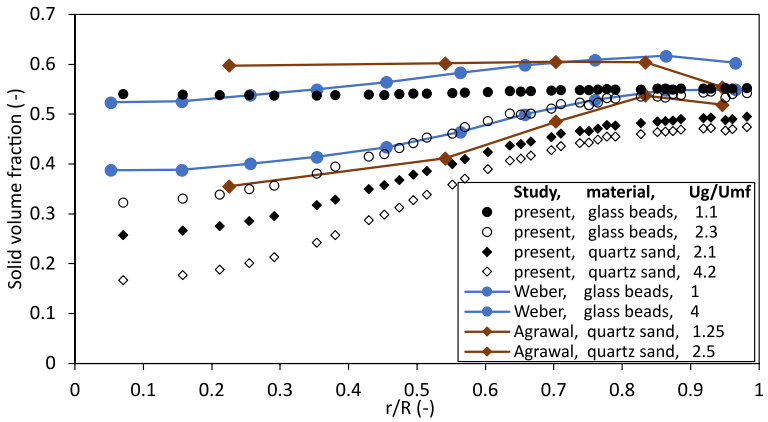

Fig. 18. Solid volume fraction results from Agrawal et al. [17] and Weber at. [16] compared with the glass beads and quartz sand from the current study (Measurement height above distributor: present work: 20 cm, Weber and Mei: 18.4 cm, Agrawal: 20.75 cm).

the unavailability in the sources and for an easier comparison of the trends. Regarding the differences in bed material and bubbling bed dimensions though, the radial trends and trends with increasing gas velocity are similar. In the Agrawal and Weber trends, the solid volume fraction decreases slightly at the wall zone for all measured velocities. This could be an indication of bubbles hugging against the wall to rise up through the bed with less resistance. However, this dip in the solid volume fraction was not observed in the results of the current study. A reason for this could be a different gas distributor design. The difference of the solid fractions from the quartz sand plots are due to different particles sizes and sphericities.

5.3. Radial bubble diameter

Fig. 19 shows the radial and axial trends of bubble diameters of quartz sand and glass beads. At all three fluidization air velocities, the greatest radial bubble diameters were measured at the radial center of the column. This is most likely due to lateral bubble coalescence in this direction. At 8 cm/s for quartz sand and 16 cm/s for glass beads both materials have a similar U_g/U_{mf} ratio of roughly 2.2, where the same bubble diameter was determined. Furthermore, at this condition the maximum radial bubble diameter for both materials is located at approximately 20 cm from the distributor plate. This is indicative of a maximum bubble size being reached, beyond which bubble splitting leads to a decrease in bubble size. The axial position of this maximum radial bubble diameter decreases with increasing fluidization air velocity, which serves as evidence of the maximum bubble size being reached closer to the distributor at higher fluidization air velocities. The radial bubble diameters increase also with increasing fluidization air velocities. This is expected, since larger bubbles are usually formed with increased airflows instead of a leaner emulsion phase [23] (p. 116). This phenomenon has also been studied extensively by Shen et al. [24], though the equivalent bubble diameter was measured instead of the radial bubble diameter. The ECVT study of Agrawal et al. [17] came to a similar conclusion, where the maximum bubble diameter was detected in a similar bed height. A suggested reason for this behavior is the segregation of fines to the top of the bed, which influences bubbles properties at different bed heights.

In comparison, the empirical correlations by Werther [25], Geldart [26], and Choi et al. [27], Kato & Wen [28] and Mori & Wen [29] all describe a linear or near-linear bubble growth with increasing axial position, as seen in Fig. 20 a. Thus, bubble splitting may be underestimated in these correlations. At lower and middle bed heights, the bubble diameters from the correlations were smaller than the measured ones. At the top of the bed, the correlations mostly agreed with the experimental data. Out of the used correlations, only the one by Mori and Wen [29] includes the bed diameter, where the bubble diameter increases, with decreasing bed diameters. Since bubbles are closer in smaller diameter beds, they reach each other faster to form larger bubbles [30]. Furthermore, none of the correlations includes the fixed bed height. The exclusion of these parameter might lead to some discrepancies between the experimental data and correlations. It is also very likely, that the main control parameters in the 3D fluxion script, the bubble exit and bubble entry limits, L_+ and L_- (as described in section 2.3) can be further optimized. This could lead to bubble diameters, closer to the ones from correlations and literature. For a better validation, comparisons with other accurate tomographic methods, like MRI would be necessary.

The bubble diameters from the present study were also compared with the ECVT studies by Agrawal et al. [17] and Weber and Mei [16] at similar U_g/U_{mf} ratios (Fig. 20 b). In comparison to the two studies, the bubble diameter, determined with the 3D fluxion method is the largest. In all three cases, the maximum diameter was detected at a bed height of around 20 cm. As the only one of the works, the bubble diameters of Weber and Mei didn't show a clear decrease after reaching a maximum value. A reason for this might be a lack of data at bed heights above 23 cm.

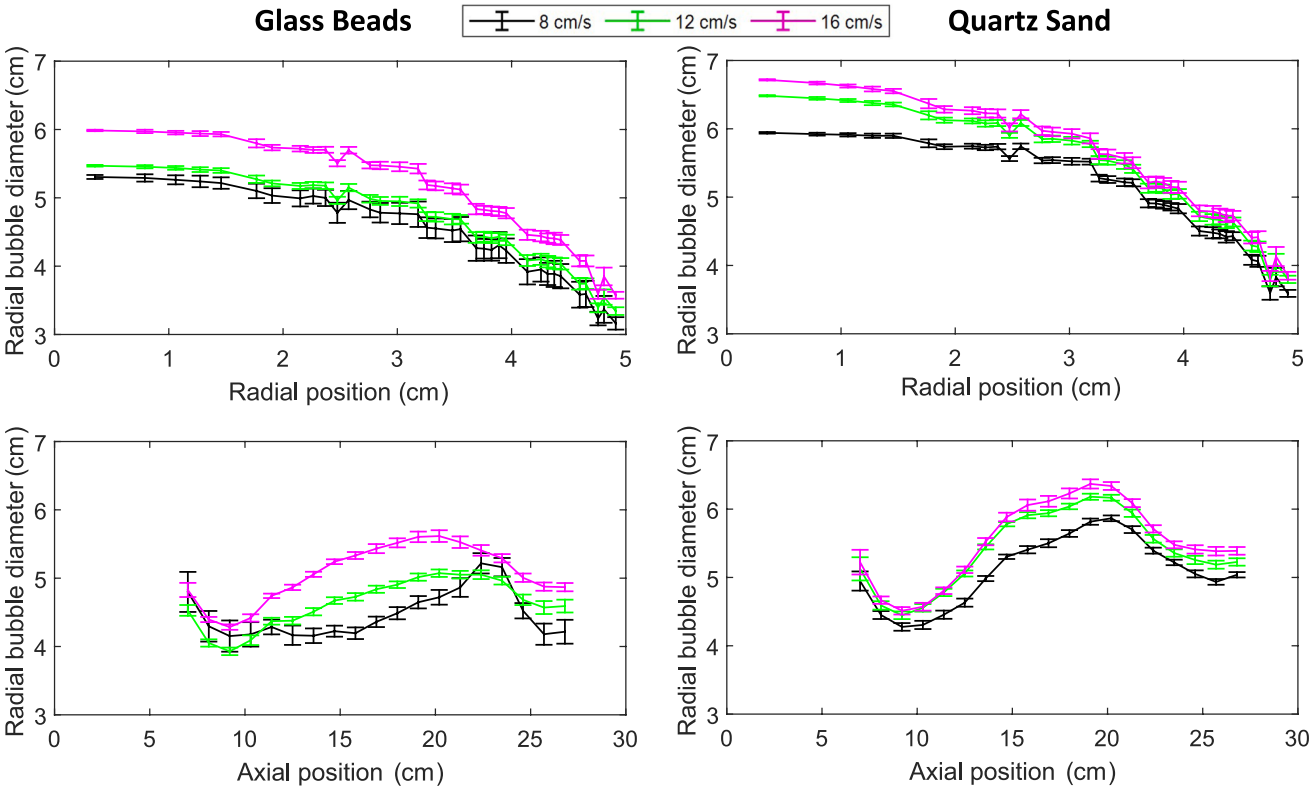

Fig. 19. Radial and axial trends of radial bubble diameter for glass beads and quartz sand for three gas velocities.

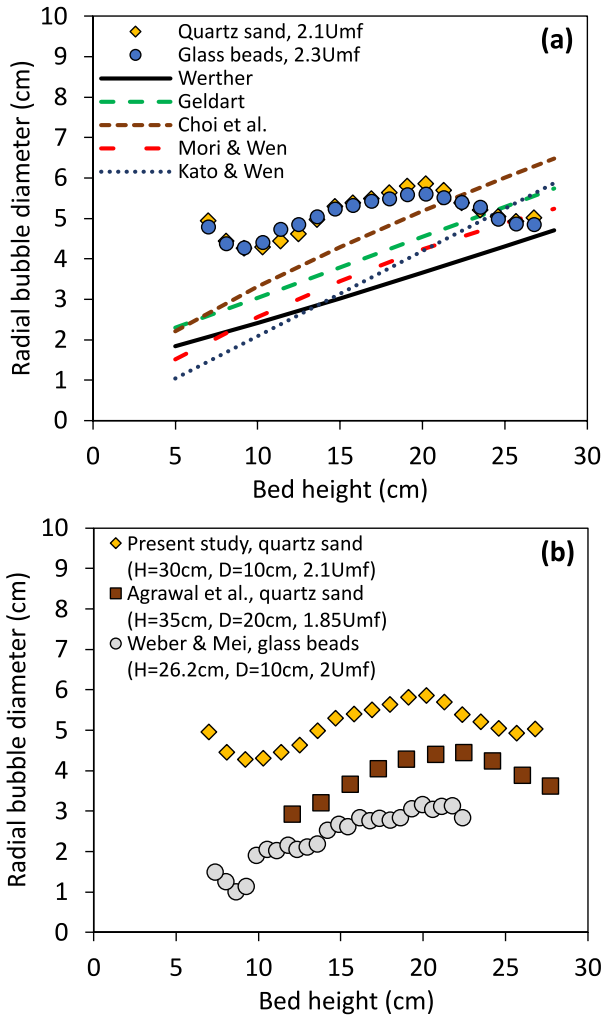

Fig. 20. (a) Bubble diameter along bed height at for experimental data with quartz sand (U_g/U_{mf} = 2.1, U_g = 8 cm/s) and glass beads (U_g/U_{mf} = 2.3, U_g = 16 cm/s), compared to various empirical correlations. For the correlations, experimental conditions for the glass beads measurement were used, (b) Axial profiles of bubble diameters compared to literature data.

5.4. Axial bubble length

Fig. 21 shows the radial and axial trends of the axial bubble length for glass beads and quartz sand. For glass beads, the axial bubble length changed only slightly across the width of the column, which indicates a low wall effect due to the high sphericity of glass beads. The axial lengths of the bubbles near the wall in the quartz sand experiments were greater and less consistent than the lengths at the center. The difference increased with increasing fluidization air velocity, which indicates that more axially elongated bubbles formed at the wall zone in the experiments with quartz sand than in those with glass beads. An explanation for this could be that the lower sphericity of the quartz sand particles allowed for increased channeling at the low-resistance wall zone. This may be favorable over increased bubbling at the radial center, where the interactions between the rough particles provide greater resistance to fluidization. With increasing axial positions, detected bubbles become increasingly elongated as they rise to the upper surface of the fluidized bed. The axial bubble length trends for quartz sand seem to show a dependence on the sensor position, which would explain the minima and maxima, as discussed in section 5.2. By comparison of the bubble lengths with the diameters, it can be concluded that bubble splitting in the bed occurs more radially than it does axially. Generally, like the bubble diameter the bubble length increases with higher gas velocities. The obtained axial bubble lengths are assumed to be overestimated, since they often reach values as high as the bed diameter. Nevertheless, since the relative trends with increasing fluidization velocities are so clear, the observed tendencies are still deemed valid and worthy of comparison with other works.

5.5. Bubble residence time

The residence times shown in Fig. 22 are equal to the average amount of time that a single voxel (1.1 cm x 0.55 cm x 0.55 cm) is occupied by a bubble. The difference between the bubble residence times at different fluidization air velocities is very small. The radial trend of the bubble residence time for glass beads shows that there is no significant change with respect to radial position. The axial trend, however, shows that the residence time increases with increasing axial position. Since the residence time is directly related to the axial bubble length, this near-linear dependence on axial position is expected. For quartz sand, the increased axial length at the wall zone also causes the bubble residence time to be slightly higher at the wall zone. This, in turn, indirectly contributes to the lower bubble frequencies observed near the wall, as shown in section 5.7.

5.6. Bubble rise velocity

The bubble rise velocity is calculated using the axial bubble length and the bubble residence time. Fig. 23 shows the radial and axial trends of the bubble rise velocities for glass beads and quartz sand. Overall, a direct dependency of the bubble rise velocity and gas velocity can be determined axially and radially. However, closer to the wall, no strong dependence on the bubble rise velocity can be seen from the trends. There is a noticeable axial dependence of the bubble rise velocity, though. The bubbles rise at greater speeds as they travel axially toward the upper surface of the fluidized bed. The axial bubble rise velocity trends also appear to show a dependence on the sensor position, which would explain the minima and maxima, as discussed earlier in section 5.2. Due to the aforementioned tendency of excess air to travel through fluidized bed as bubbles rather than within the emulsion phase, an increase in fluidization air velocity will always increase the bubble rise velocity until the slugging regime is reached. After the diameter of the bubbles reaches approximately 60 % of the diameter of the column, slugs may start to form, at which point the linear dependency of the bubble rise velocity on the bubble size will dissipate. This leads to a decrease in bubble rise velocity dependence on axial position [23] (p. 149), as it is observed in this work. The ECVT study of Agrawal et al. [17] yielded a similar result, where the bubble rise velocity was between 55 and 65 cm/s in a 10 – 25 cm axial position range for quartz sand at 1.85 U_g/U_{mf}. Although a column with a greater diameter and a higher H_{bed}/D_{bed} ratio were used, the results are still similar.

5.7. Bubble frequency

Fig. 24 shows the radial and axial trends of the bubble frequency for glass beads and quartz sand. These values are equal to the average number of bubbles that pass through a single voxel per second. Like the bubble rise velocity, this property is related to the axial bubble length and the bubble residence time. Unlike the bubble rise velocity, however, this dependency is indirect since the time between the exit of one bubble and the entry of another has also a great effect on the measured bubble frequency.

Like the residence time, the measured bubble frequencies are almost independent of the gas velocity. For glass beads the bubble frequencies only slightly depend on the radial position. The reason for this might be the high sphericity, leading to a more uniform bubble distribution. Additionally, since glass beads were fluidized at gas velocities, much closer to U_{mf}, the wall effect is also expected to be smaller. At the two

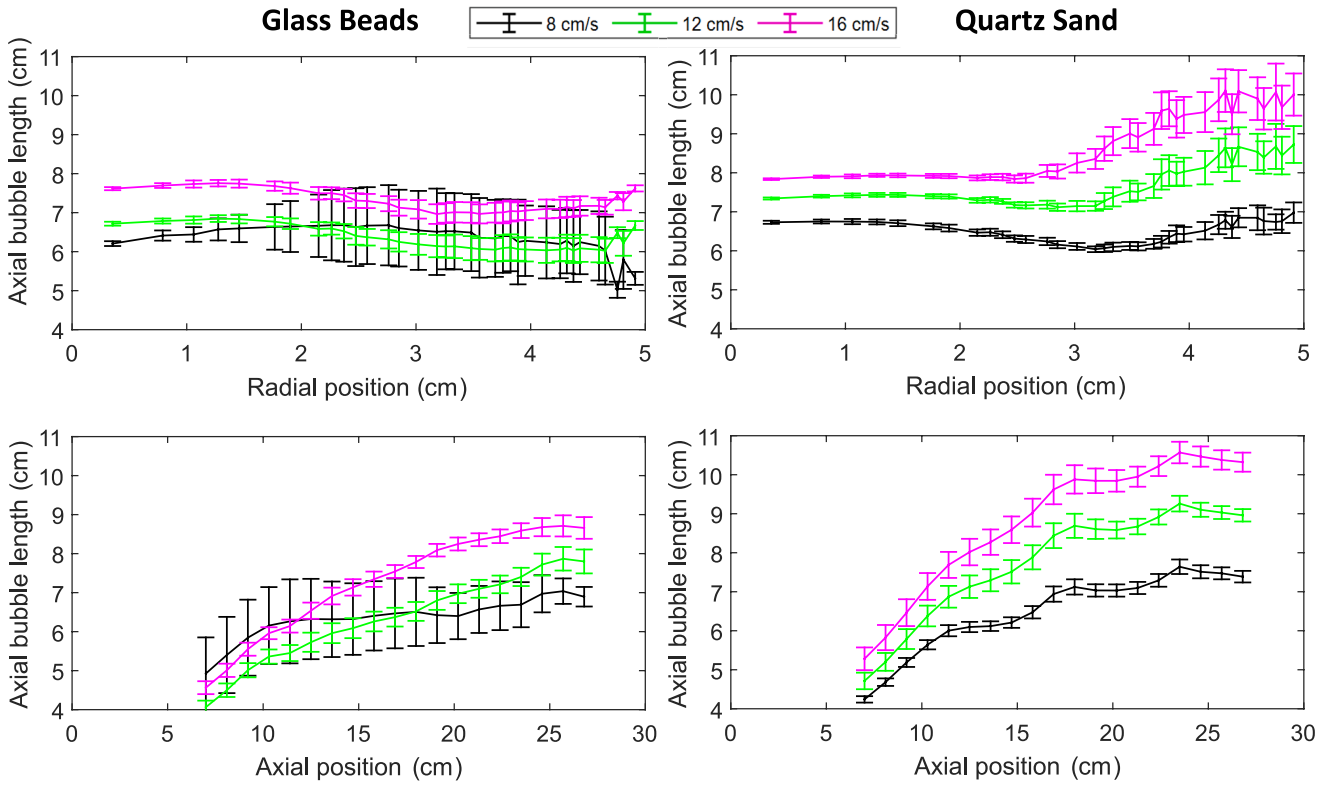

Fig. 21. Radial and axial trends of axial bubble length for glass beads, quartz sand for three gas velocities.

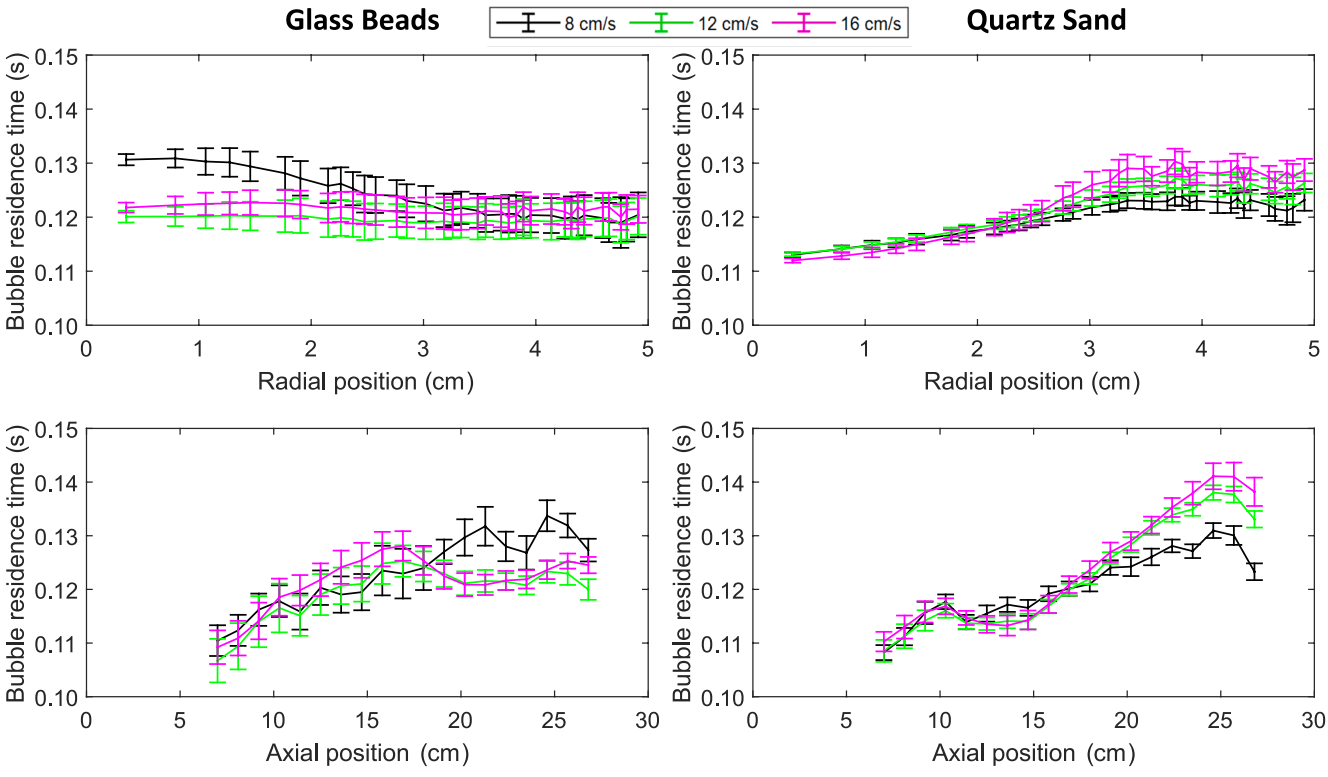

Fig. 22. Radial and axial trends of bubble residence time for glass beads and quartz sand.

highest fluidization velocities, the frequency is increased at the radial center of the column. This is likely due to lateral bubble movement from the wall to the center. Contrarily, for quartz sand, a strong influence on the radial position is seen. The highest bubble frequencies were observed at the center of the column, while the lowest were close to the wall. This can be attributed the lower sphericity of quartz sand, leading

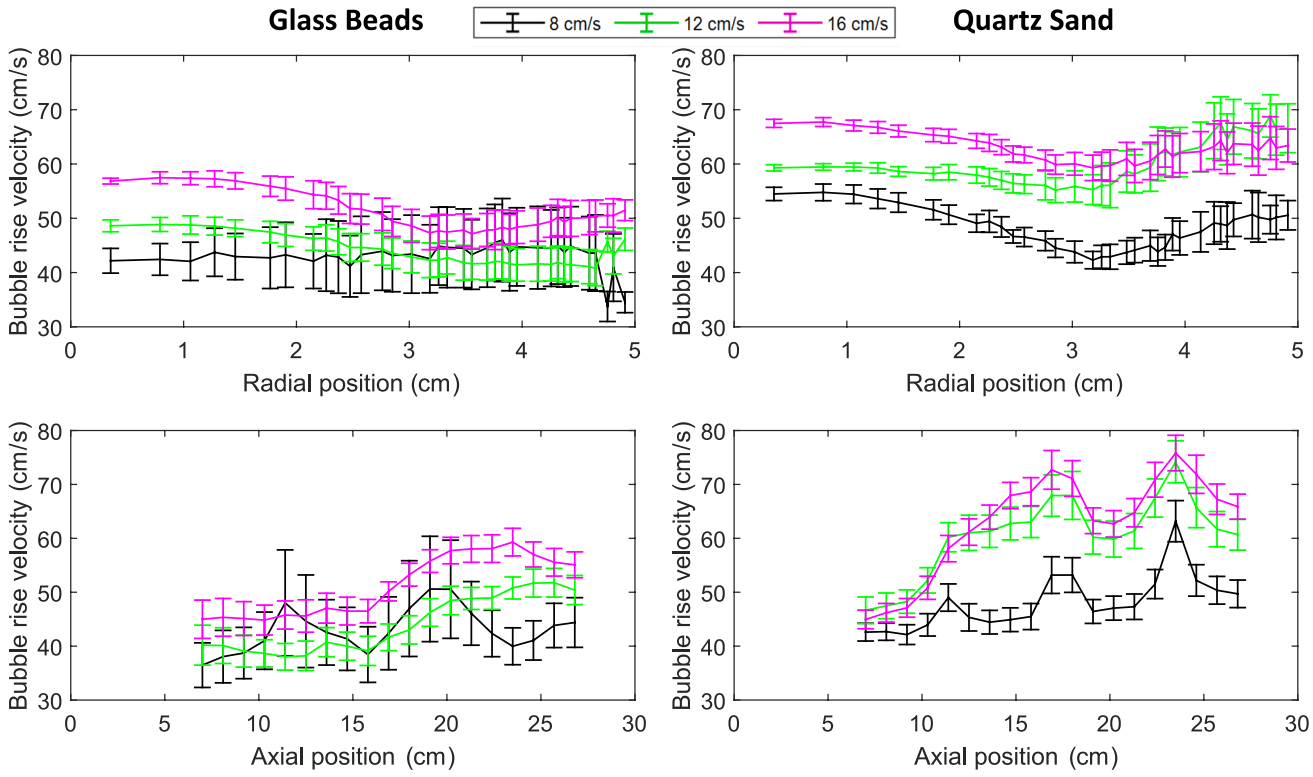

Fig. 23. Radial and axial trends of bubble rise velocity for glass beads and quartz sand for three gas velocities.

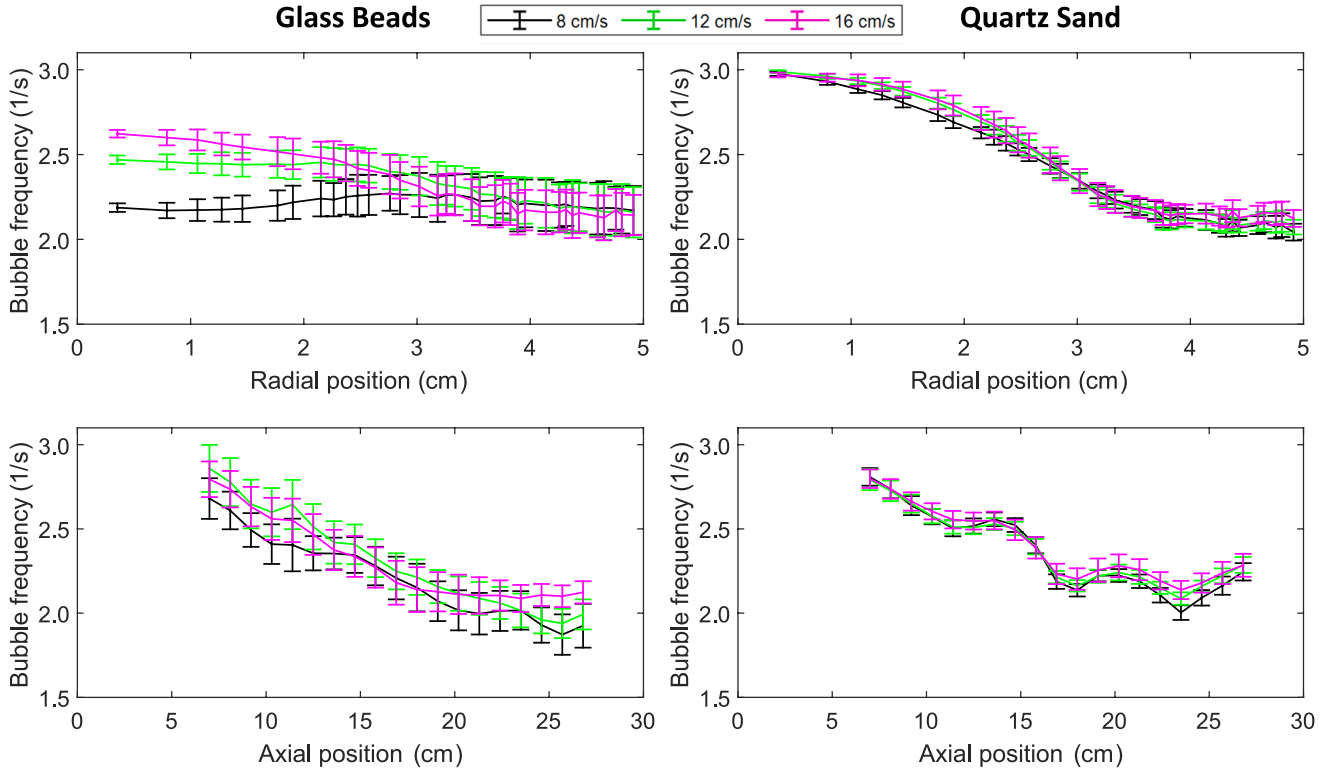

Fig. 24. Radial and axial trends of bubble frequency for glass beads and quartz sand for three gas velocities.

to stronger particle–particle and particle–wall forces. Thus, at the column center, a greater quantity of bubbles was detected.

A strong dependence exists between the bubble frequency and the axial position. As the bubbles rise axially to the upper surface of the fluidized bed, they coalesce, which leads to fewer bubbles. Since these larger, newly formed bubbles will not rise with lower velocity through

the bed, the total bubble count per unit time must decrease. This results in a steady decrease in bubble frequency as a function of axial position. For quartz sand the axial bubble frequency trends also appear to show a dependence on the sensor position, which would explain the observed minima and maxima, as discussed before in section 5.2.

Similar results were reported by Agrawal et al. [17]. The bubble frequencies from the Agrawal study with quartz sand were measured for the entire radial cross-section, while the values from the current study were measured for each voxel and averaged across the entire radial cross–section. The iterative axial bubble threshold method used in the Agrawal study does not allow for multiple bubbles to be detected at a single axial position for a given frame. These two differences may contribute to discrepancies between the ranges of results. Nevertheless, the results from both studies are very similar, with the frequency dropping from 3.0 to 3.5 Hz at an axial position of 7 cm in this work to 2.5—3.25 Hz at 27 cm axial position in the Agrawal dataset. Furthermore, the frequency decreased nearly linearly across the measured axial ranges.

6. Conclusion

A novel method for detection and sizing of bubbles in fluidized beds was developed to more fully utilize the potential of ECVT. It detects bubbles by measuring the rate of change of the solid volume fraction for every voxel and frame. The results indicate that the detected bubble boundaries are similar, to those detected via methods with a single global threshold value for the bubble detection limit, like Agrawal et al. [17]. and Weber and Mei [16]. The detection method can potentially be used with other measurement techniques that produce four-dimensional arrays of solid volume fractions like MRI.

The phase detection method was tested with glass beads and quartz sand in a bubbling fluidized bed (D = 10 cm, $H_{bed}/D_{bed} = 3$) at three fluidization velocities. For both particle systems, significant similarities with results from publications with similar experimental setups were found. This includes radial and axial trends for solid volume fraction, radial bubble diameter, bubble frequency, and bubble rise velocity. Furthermore, due to the three-dimensional nature of the novel bubble detection technique, insight into the directional tendencies of detected bubbles was gained. For example, bubble migration toward the radial center of the bed, as well as radial and axial bubble coalescence and splitting, are more clearly evident from the trends, produced with this method.

CRediT authorship contribution statement

Brigham Watson: Investigation, Methodology, Validation, Visualization, Writing – original draft. **Lennard Lindmüller:** Methodology, Supervision, Visualization, Writing – original draft, Writing – review & editing. **Stefan Heinrich:** Project administration, Supervision. **Jörg Theuerkauf:** Supervision. **Yuan Yao:** Supervision. **Yi Fan:** Supervision.

Declaration of competing interest

The authors declare that they have no known competing financial interests or personal relationships that could have appeared to influence the work reported in this paper.

Data availability

Data will be made available on request.

Acknowledgments

Financial support was provided by the Dow Chemical Company, United States award no. 223278AW.

References

[1] T. McKeen, T. Pugsley, Simulation and Experimental Validation of a Freely Bubbling Bed of FCC Catalyst 129 (2003) 139–152, https://doi.org/10.1016/S0032-5910(02)00294-2.
[2] T.C. Chandrasekera, Y. Li, D. Moody, M.A. Schnellmann, J.S. Dennis, D.J. Holland, Measurement of bubble sizes in fluidised beds using electrical capacitance tomography, Chemical Engineering Science 126 (2015) 679–687, https://doi.org/10.1016/j.ces.2015.01.011.
[3] C.E. Agu, L.-A. Tokheim, M. Eikeland, B.M. Moldestad, Improved models for predicting bubble velocity, bubble frequency and bed expansion in a bubbling fluidized bed, Chemical Engineering Research and Design 141 (2019) 361–371, https://doi.org/10.1016/j.cherd.2018.11.002.
[4] I. Hulme, A. Kantzas, Determination of bubble diameter and axial velocity for a polyethylene fluidized bed using X-ray fluoroscopy, Powder Technology 147 (2004) 20–33, https://doi.org/10.1016/j.powtec.2004.08.008.
[5] M. Stein, Y. Ding, J. Seville, D. Parker, Solids motion in bubbling gas fluidised beds, Chemical Engineering Science 55 (2000) 5291–5300, https://doi.org/10.1016/S0009-2509(00)00177-9.
[6] A. Penn, C.M. Boyce, T. Kovar, T. Tsuji, K.P. Pruessmann, C.R. Müller, Real-time magnetic resonance imaging of bubble behavior and Particle velocity in fluidized beds, Ind. Eng. Chem. Res. 57 (2018) 9674–9682, https://doi.org/10.1021/acs.iecr.8b00932.
[7] W. Warsito, M. Qussai, L.-S. Fan, Electrical capacitance volume tomography, IEEE SENSORS JOURNAL 7 (2007) 525–535, https://doi.org/10.1109/JSEN.2007.891952.
[8] Q. Marashdeh, L.-S. Fan, B. Du, W. Warsito, Electrical capacitance tomography – a perspective, Ind. Eng. Chem. Res. 47 (2008) 3708–3719, https://doi.org/10.1021/ie0713590.
[9] W.C. Chew, Waves and Fields in Inhomogeneous Media, Vol. 16, John Wiley & Son, 1999.
[10] C.G. Xie, S.M. Huang, M.S. Beck, B.S. Hoyle, R. Thorn, C. Lenn, D. Snowden, Electrical capacitance tomography for flow imaging: system model for development of image reconstruction algorithms and design of primary sensors, IEE proc, F Radar Signal Process. UK 139 (1992) 89, https://doi.org/10.1049/ip-g-2.1992.0015.
[11] W.Q. Yang, D.M. Spink, T.A. York, H. McCann, An image-reconstruction algorithm based on landweber's iteration method for electrical-capacitance tomography, Meas. Sci. Technol. 10 (1999) 1065–1069, https://doi.org/10.1088/0957-0233/10/11/315.
[12] W.W. Warsito, L.-S. Fan, Neural network multicriteria optimization image reconstruction technique (NN-MOIRT) for linear and non-linear process tomographic imaging of two- and three-phase flow systems, Chem. Eng. Proc 48 (2003) 663–674, https://doi.org/10.1016/S0255-2701(02)00204-0.
[13] J.J. Hopfield, D. Tank, Neural computation of decisions in optimization problems, Biol. Cybern. 52 (1985) 141–152, https://doi.org/10.1007/BF00339943.
[14] T.W. Asegehegn, M. Schreiber, H.J. Krautz, Investigation of bubble behavior in fluidized beds with and without immersed horizontal tubes using a digital image analysis technique, Powder Technology 210 (2011) 248–260, https://doi.org/10.1016/j.powtec.2011.03.025.
[15] B. Han, Z. Sun, J. Zhu, Z. Fu, X. Kong, S. Barghi, Bubble dynamics in 2-D gas–solid fluidized bed with Geldart a or Geldart B particles by image processing method, Can J Chem Eng 100 (2022) 3588–3599, https://doi.org/10.1002/cjce.24391.
[16] J.M. Weber, J.S. Mei, Bubbling fluidized bed characterization using electrical capacitance volume tomography (ECVT), Powder Technology 242 (2013) 40–50, https://doi.org/10.1016/j.powtec.2013.01.044.
[17] V. Agrawal, Y.H. Shinde, M.T. Shah, R.P. Utikar, V.K. Pareek, J.B. Joshi, Estimation of bubble properties in bubbling fluidized bed using ECVT measurements, Ind. Eng. Chem. Res. 57 (2018) 8319–8333, https://doi.org/10.1021/acs.iecr.8b00349.
[18] J. Werther, O. Molerus, The local structure of gas fluidized beds —I, A Statistically Based Measuring System, International Journal of Multiphase Flow 1 (1973) 103–122, https://doi.org/10.1016/0301-9322(73)90007-4.
[19] J.W. Chew, C.M. Hrenya, Link between bubbling and segregation patterns in gas-fluidized beds with continuous size distributions, AIChE Journal 57 (2011) 3003–3011, https://doi.org/10.1002/aic.12507.
[20] J.N. Sines, B.J. Straiton, C.E. Zuccarelli, Q.M. Marashdeh, F.L. Teixeira, L.-S. Fan, B.J. Motil, Study of gas-water flow inside of a horizontal passive cyclonic gas-liquid phase separator system using displacement-current phase tomography, Gravitational and Space Research 6 (2018) 28–43, https://doi.org/10.2478/gsr-2018-0008.
[21] Y.T. Makkawi, P.C. Wright, Electrical capacitance tomography for conventional fluidized bed measurements—remarks on the measuring technique, Powder Technology 148 (2004) 142–157, https://doi.org/10.1016/j.powtec.2004.09.006.
[22] Y.T. Makkawi, P.C. Wright, Tomographic analysis of dry and semi-wet bed fluidization: the effect of small liquid loading and particle size on the bubbling behaviour, Chemical Engineering Science 59 (2004) 201–213, https://doi.org/10.1016/j.powtec.2004.09.006.
[23] D. Kunii, O. Levenspiel, Fluidization engineering, second ed.,, Butterworth-Heinemann, Stoneham, MA, USA, 1991.
[24] L. Shen, F. Johnsson, B. Leckner, Digital image analysis of hydrodynamics two-dimensional bubbling fluidized beds, Chemical Engineering Science 59 (2004) 2607–2617, https://doi.org/10.1016/j.ces.2004.01.063.
[25] J. Werther, Effect of gas distributor on hydrodynamics of gas fluidized beds, german, Chem. Eng. 1 (1978) 166–174.

[26] D. Geldart, The effect of particle size and size distribution on the behaviour of gas-fluidised beds, Powder Technology 6 (1972) 201–215, https://doi.org/10.1016/0032-5910(72)83014-6.
[27] J.-H. Choi, J.-E. Son, S.-D. Kim, Bubble size and frequency in gas fluidized beds, J. Chem. Eng. Japan / JCEJ 21 (1988) 171–178, https://doi.org/10.1252/jcej.21.171.
[28] K. Kato, C.Y. Wen, Bubble assemblage model for fluidized bed catalytic reactors, Chemical Engineering Science 24 (1969) 1351–1369, https://doi.org/10.1016/0009-2509(69)85055-4.
[29] S. Mori, C.Y. Wen, Estimation of bubble diameter in gaseous fluidized beds, AIChE Journal 21 (1975) 109–115, https://doi.org/10.1002/aic.690210114.
[30] J. Werther, Influence of the bed diameter on the hydrodynamics of gas fluidized beds, AIChE Symp. Ser. 70 (141) (1974) 53–62.